



Amphibole and apatite insights into the evolution and mass balance of Cl and S in magmas associated with porphyry copper deposits

Cyril Chelle-Michou^{1,2} · Massimo Chiaradia¹

Received: 5 May 2017 / Accepted: 25 October 2017 / Published online: 21 November 2017
© The Author(s) 2017. This article is an open access publication

Abstract

Chlorine and sulfur are of paramount importance for supporting the transport and deposition of ore metals at magmatic–hydrothermal systems such as the Corocochuayco Fe–Cu–Au porphyry–skarn deposit, Peru. Here, we used recent partitioning models to determine the Cl and S concentration of the melts from the Corocochuayco magmatic suite using apatite and amphibole chemical analyses. The pre-mineralization gabbrodiorite complex hosts S-poor apatite, while the syn- and post-ore dacitic porphyries host S-rich apatite. Our apatite data on the Corocochuayco magmatic suite are consistent with an increasing oxygen fugacity (from the gabbrodiorite complex to the porphyries) causing the dominant sulfur species to shift from S^{2-} to S^{6+} at upper crustal pressure where the magmas were emplaced. We suggest that this change in sulfur speciation could have favored S degassing, rather than its sequestration in magmatic sulfides. Using available partitioning models for apatite from the porphyries, pre-degassing S melt concentration was 20–200 ppm. Estimates of absolute magmatic Cl concentrations using amphibole and apatite gave highly contrasting results. Cl melt concentrations obtained from apatite (0.60 wt% for the gabbrodiorite complex; 0.2–0.3 wt% for the porphyries) seems much more reasonable than those obtained from amphibole which are very low (0.37 wt% for the gabbrodiorite complex; 0.10 wt% for the porphyries). In turn, relative variations of the Cl melt concentrations obtained from amphibole during magma cooling are compatible with previous petrological constraints on the Corocochuayco magmatic suite. This confirms that the gabbrodioritic magma was initially fluid undersaturated upon emplacement, and that magmatic fluid exsolution of the gabbrodiorite and the pluton rooting the porphyry stocks and dikes were emplaced and degassed at 100–200 MPa. Finally, mass balance constraints on S, Cu and Cl were used to estimate the minimum volume of magma required to form the Corocochuayco deposit. These three estimates are remarkably consistent among each other (ca. 100 km³) and suggest that the Cl melt concentration is at least as critical as that of Cu and S to form an economic mineralization.

Keywords Apatite · Amphibole · Chlorine · Sulfur · Porphyry copper deposit · Magma volume

Communicated by Hans Keppler.

Electronic supplementary material The online version of this article (<https://doi.org/10.1007/s00410-017-1417-2>) contains supplementary material, which is available to authorized users.

✉ Cyril Chelle-Michou
Cyril.chelle-michou@bristol.ac.uk

¹ Department of Earth Sciences, University of Geneva, rue des Maraîchers 13, 1205 Geneva, Switzerland

² School of Earth Sciences, University of Bristol, Wills Memorial Building, Queens Road, Bristol BS8 1RJ, UK

Introduction

The formation of porphyry copper systems critically depends on the availability of volatiles (e.g., H₂O, Cl, S) and metals (e.g., Cu, Au) in the silicate melt at the time of fluid saturation and exsolution. These elements are usually sourced from andesitic to dacitic magmas that undergo outgassing upon cooling and crystallization at upper crustal depth, and subsequently transported to higher crustal levels where extensive sulfide precipitation might occur if appropriate conditions are met (Hedenquist and Lowenstern 1994; Dreher et al. 2005; Sillitoe 2010; Pettke et al. 2010; Simon and Ripley 2011; Chelle-Michou et al. 2017). Importantly, chlorine and sulfur are critical elements of ore-forming fluids due to their capacity to form ligands with ore metals (e.g.,

Cu, Au, Pb, Zn, Fe, Mo) as well as with other cations (e.g., H^+ , K^+ , Na^+ , Ca^+) which permit their transport to the site of ore deposition and cause hydrothermal alteration (Candela and Holland 1984; Williams et al. 1995, 1997; Frank et al. 2003; Simon et al. 2004, 2006; Williams-Jones and Heinrich 2005; Zajacz and Halter 2009; Zajacz et al. 2010, 2012; Kouzmanov and Pokrovski 2012; Pokrovski et al. 2015; Tatitch and Blundy 2017).

The study of volatiles in crystalline magmatic rocks such as those associated with porphyry systems is hindered by the fact that these rocks have lost the majority of their volatile budget during degassing and that the resulting mineral assemblage and mineral chemistry in the crystalline rock would be only minimally influenced by these elements. In addition, melt inclusions that might have preserved the volatile content at magmatic conditions are not always available (or large enough) within the crystal cargo of magmatic rocks. Nevertheless, common hydrous minerals such as biotite, amphibole and apatite may keep record of the evolution of various volatiles in the magma from which they crystallized (e.g., Coulson et al. 2001; Parat et al. 2011a; Zhang et al. 2012, 2017; Rasmussen and Mortensen 2013; Chambefort et al. 2013; Van Hoose et al. 2013; Teiber et al. 2015; Scott et al. 2015; Bao et al. 2016).

Here, we aim at decoding the Cl and S record of amphibole and apatite from the magmatic suite associated with the Eocene Coroccohuayco porphyry-skarn Cu (–Au–Fe)

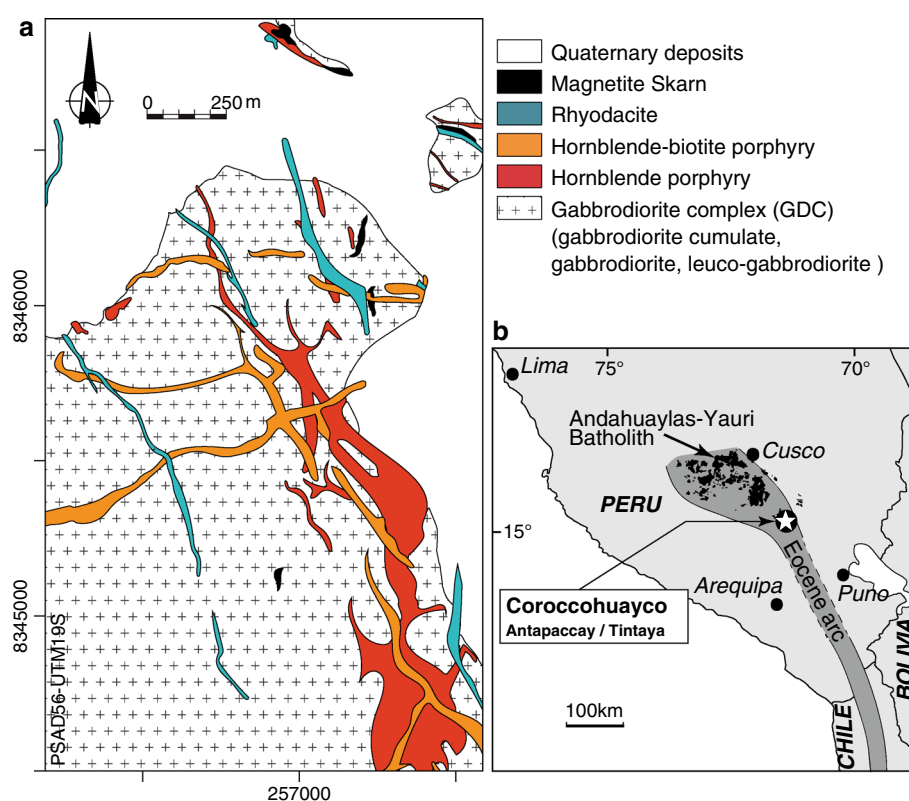
deposit, Peru. This system evolved from gabbroic to rhyodacitic composition through 5 Ma (Chelle-Michou et al. 2015a) and represents an opportunity to understand the evolution of volatiles in a long-lived magmatic system and try to identify the tipping point leading to the formation of an economic mineralization. These results can further be used to obtain mass balance constraints on the volume of magma required to form such a deposit.

Geological background

The Coroccohuayco Fe–Cu–Au porphyry–skarn deposit is located at the southern tip of the Andahuaylas–Yauri batholith of southern Peru, in the Tintaya mining district (which includes Tintaya, Antapaccay, Quechua, Ccatun Pucara; Fig. 1). This calc-alkaline batholith represents the plutonic root of the subduction-related Eocene magmatic arc and is emerging as an important Cu–Au metallogenic province. Magmatism and hydrothermal activity at Coroccohuayco is polyphased, and lasted from 41 to 35 Ma (Chelle-Michou et al. 2014, 2015b). The geochemical and petrological features of the Coroccohuayco magmatic suite have previously been described in Chelle-Michou et al. (2015a) and are summarized below.

Magmatic activity started at 40.5–40.2 Ma with the emplacement of a heterogeneous sill-shaped body of gabbro and diorite termed the gabbrodiorite complex (Fig. 1).

Fig. 1 **a** Geological map of the Coroccohuayco deposit, Peru. The main skarn body is located below the sill-shaped gabbrodiorite complex at an average of 200 m depth. Adapted from Chelle-Michou et al. (2014). **b** Location of the Andahuaylas–Yauri Batholith and of the Tintaya–Coroccohuayco mining district



Using mineralogical and geochemical criteria, four phases could be identified within this complex: a gabbrodiorite, a gabbrodiorite “cumulate”, a leuco-gabbrodiorite and subordinate anorthosite. The first two phases are by far the most voluminous (> 95 vol%) and will be investigated in the present study. Both phases are made of euhedral normally zoned plagioclase (An90–30), poikilitic hornblende, Fe–Ti oxides (magnetite and ilmenite, both with sub-solidus exsolution lamellae), and interstitial quartz \pm K-feldspar \pm biotite (Fig. 2a, b). Resorbed clinopyroxene and/or orthopyroxene is often found in the core of poikilitic hornblende. Accessory minerals consist of apatite, zircon and occasional titanite and magmatic sulfides. Compared to the gabbrodiorite, the gabbrodiorite “cumulate” has more abundant hornblende and pyroxene, and less plagioclase (more calcic on average), is less silicic (ca. 48 wt% SiO₂ versus 51 wt%), has lower REE, Zr and P₂O₅ abundances and features a positive Eu anomaly. Chelle-Michou et al. (2015a) concluded that the gabbrodiorite “cumulate” represents an immature cumulate of early crystallized mineral phases (high-An plagioclase, pyroxenes) with an interstitial liquid that was depleted in incompatible elements compared to that of the gabbrodiorite. Signs of sub-solidus hydrothermal alteration are seldom observed in

the gabbrodiorite complex and only the least altered samples were considered for this study.

After a nearly 5 Ma-long gap, magmatic activity resumed at 35.6 Ma with the successive emplacement (as stocks and dikes) of the hornblende and hornblende–biotite porphyries, both of dacitic composition (Fig. 1), and the coeval formation of the Fe–Cu–Au porphyry–skarn mineralization (Chelle-Michou et al. 2015b). This major magmatic–hydrothermal event was closely followed by the emplacement of rhyodacite porphyry dikes (Fig. 1). Despite being affected by a pervasive and destructive alteration of mafic minerals, these dikes crosscut the mineralization and the first two porphyries. All the porphyries feature a similar mineralogy dominated by An30–10 plagioclase, hornblende, biotite, magnetite and K-feldspar phenocrysts (Fig. 2c, d). The groundmass (46–56 vol%) is dominated by a microcrystalline patchwork of plagioclase, quartz and K-feldspar. Accessory minerals consist of titanite, apatite and zircon. No magmatic sulfide or sulfate phase could be observed in the porphyries. With the timing of emplacement, the porphyries evolve to more silicic compositions (from 63 to 68 wt% SiO₂) and develop an increasingly higher Sr/Y signature (from 50 to 110). Geochemical modeling has suggested

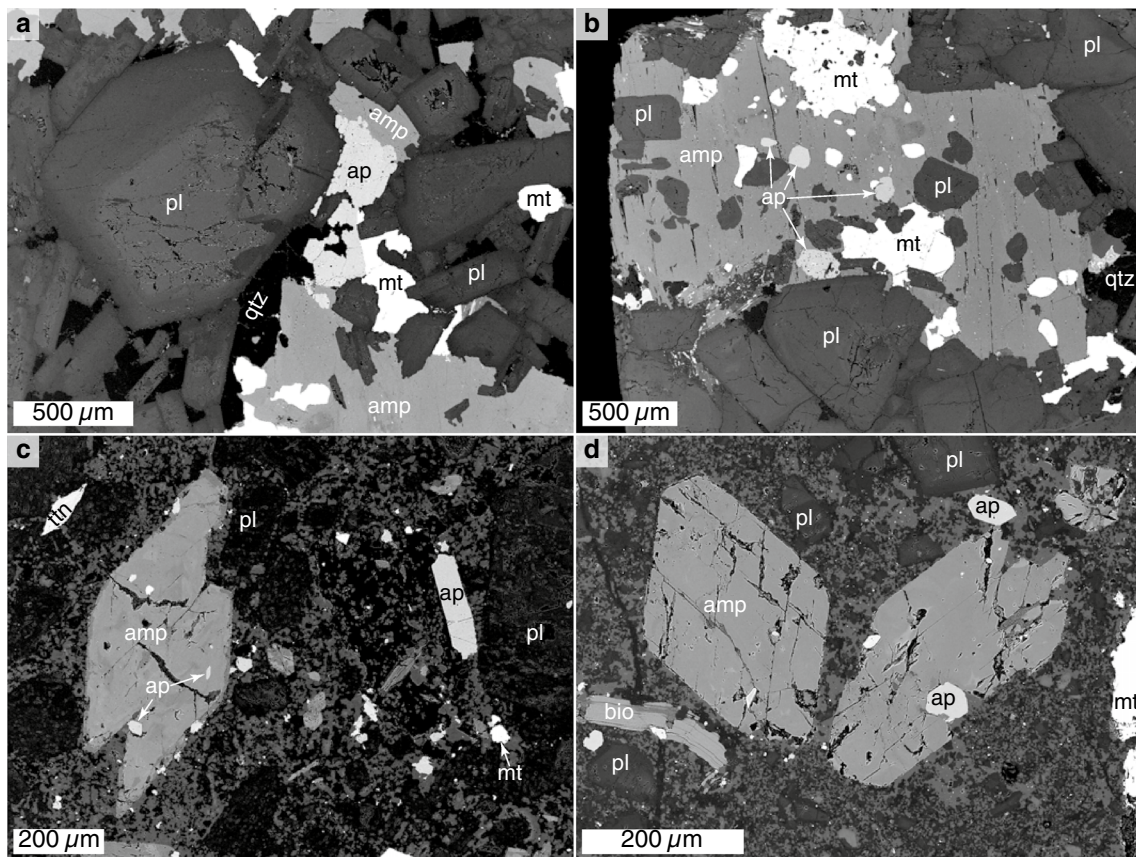


Fig. 2 Back-scattered electron SEM images showing typical occurrences of amphibole and apatite in **a, b** the gabbrodiorite complex and **c, d** the porphyries. *Amp* amphibole, *ap* apatite, *bio* biotite, *mt* magnetite, *pl* plagioclase, *qtz* quartz, *tn* titanite

that the chemistry of the porphyries results from a long-lived evolution within a deep crustal hot zone dominated by crystal fractionation, followed by crustal assimilation in the mid to upper crust. High-precision U–Pb zircon dating of the rhyodacite revealed that it resulted from the remelting of a proto-pluton emplaced at 36.1 Ma (Chelle-Michou et al. 2014). It has been inferred that this melting event was contemporaneous with the emplacement of the porphyries and was triggered by the emplacement and degassing of a large pluton in the upper crust (Chelle-Michou et al. 2014, 2015a).

Analytical methods for apatite

Prior to analysis, apatite was identified on thin sections and imaged by backscattered electron (BSE) microscopy. Selected apatite crystals were further imaged by “cold” optical cathodoluminescence (CL) to reveal internal zoning. Apatite chemistry was determined on a JEOL® JXA 8200 electron microprobe equipped with five wavelength-dispersive spectrometers at the University of Lausanne (Switzerland). Analysis of apatite is known to be problematic due to the migration of halogens during analysis, depending on the crystallographic orientation of the apatite with respect to the electron beam (Stormer et al. 1993; Goldoff et al. 2012; Stock et al. 2015). To accurately measure both halogens (Cl and F) and trace elements (e.g., La, Ce, Y, Sr) in apatite, we successively employed a low-intensity (LI) and a high-intensity (HI) analytical protocol. Only a representative subset of apatite crystals analyzed with the LI method was subsequently analyzed with the HI method. A representative selection of apatite data is presented in Table 1 and the complete dataset is given in the Supplementary Material 1.

The LI analytical routine was designed to optimize halogen measurement (minimize diffusion) following the method proposed by Goldoff et al. (2012) which includes a 10 kV acceleration voltage, a 4 nA electron beam current and a 10 µm spot diameter. These settings were shown to minimize halogen migration even when the electron beam was parallel to the apatite *c* axis (Goldoff et al. 2012). The HI method was optimized for the measurement of the trace elements and includes a 15 kV acceleration voltage, 40 nA electron beam current and a 15 µm spot diameter. In both cases, F and Cl were analyzed first. The details of each analytical setup are presented in Supplementary Material 2.

In LI conditions, detection limits are typically in the range of ~ 200–300 ppm for Na, Mg, S and F, ~ 800–900 ppm for La, Ce, Fe and Sr, ~ 500 ppm for Y, and ~ 120 ppm for Cl (Supplementary Material 2). HI conditions yield detection limits of ~ 50–150 ppm for Na, Fe, S, Si and Cl, ~ 250–300 ppm for La, Ce and Y, and ~ 500 ppm for F and Sr (Supplementary Material 2). The analytical accuracy and precision were estimated by repeated analyses of the Durango apatite during each analytical session. Our

microprobe data for the Durango apatite show good agreement with published values for all elements (Supplementary Material 2; Young et al. 1969). The precision and accuracy of analyses are typically $\leq 1\%$ for Ca and P, and $\leq 6\%$ for F and Cl irrespective of the method used. Relative analytical precision for the most enriched trace elements in the Durango apatite (S, Na, Si, La and Ce) was generally around 10–30% for LI and 3–10% for HI. In turn, measurements of low-concentration trace elements (Fe, Mg, Y and Sr) have lower precisions around 30–50%. Mn concentration of the Durango apatite being similar to the limit of detection with the HI method, the accuracy and precision of Mn analyses in apatite from Corocchohuayco (more enriched than the Durango apatite) cannot be evaluated. Nevertheless, the good precision and accuracy of all other elements suggest that Mn analyses are likely reliable.

Comparison of high- and low-intensity analytical methods

Overall, both analytical techniques show good accuracy on the Durango apatite standard. As expected, the HI method has lower limits of detection for the trace elements we investigated compared to the LI method (Supplementary Material 2). Interestingly, both methods accurately measure the halogen concentrations of the Durango apatite (Fig. 3). However, this apatite standard corresponds compositionally almost to the pure fluorapatite pole, a composition that is not always representative of our samples (Fig. 3). A comparison of the halogen concentrations of apatite from Corocchohuayco analyzed with both techniques reveals that the HI method systematically returns higher F concentrations than the LI method (by ca. 15%) while the Cl concentration is equivalent (Fig. 3), irrespective of the orientation of the crystal. This is similar to observations by Stock et al. (2015) who reports F surface enrichment of apatite exposed to EMP electron beam. Due to the well-documented halogen diffusion in apatite (Stormer et al. 1993; Goldoff et al. 2012; Stock et al. 2015), we consider the concentrations measured with the LI method as more accurate in addition to being more precise. No such systematic difference between the LI and HI method could be observed for the other elements.

Mineral chemistry

Apatite

Apatite formulae were calculated on the basis of 16 cations. OH was calculated by difference, assuming that the F–Cl–OH site is completely filled.

Apatite grains are essentially homogeneous in terms of F and Cl content even for those showing zoned CL textures (Fig. 3). We could not identify any systematic difference

Table 1 Representative apatite composition from the Corocochuayco magmatic suite

Unit	Gabbrodiorite “cumulate”	Gabbrodiorite			Hornblende porphyry	Hornblende–biotite porphyry		Rhyodacite			
Sample	10CC61	10CC55	10CC09	10CC09	10CC64	11CC54	11CC54	11CC17	11CC17	11CC17	11CC17
Spot	apC1	apD2	apA2	apBCDE1	apE3	apD5	apF3	apH1	apK5	apH9	apJ4
Microprobe method	LI	LI	LI	HI	LI	LI	HI	LI	LI	HI	HI
(wt%)											
P ₂ O ₅ (wt%)	41.15	40.57	41.90	41.75	41.53	41.99	41.66	41.61	41.09	42.25	40.70
SiO ₂ (wt%)	0.22	0.16	0.15	0.11	0.09	0.09	0.12	0.09	0.20	0.07	0.32
FeO (wt%)	0.44	0.41	0.00	0.14	0.26	0.03	0.07	0.13	0.21	0.06	0.12
MgO (wt%)	0.03	0.04	0.02	0.00	0.02	0.02	0.00	0.00	0.03	0.00	0.02
CaO (wt%)	55.80	57.23	56.25	54.96	56.67	56.01	55.22	56.31	54.78	55.32	54.71
Na ₂ O (wt%)	0.03	0.01	0.01	0.02	0.08	0.08	0.09	0.07	0.38	0.09	0.37
SO ₃ (wt%)	0.05	0.04	0.02	0.00	0.21	0.21	0.19	0.18	0.98	0.20	1.18
SrO (wt%)	0.13	0.00	0.00	0.00	0.10	0.07	0.17	0.10	0.23	0.16	0.20
Y ₂ O ₃ (wt%)	0.08	0.14	0.00	0.00	0.00	0.02	0.03	0.00	0.06	0.03	0.04
La ₂ O ₃ (wt%)	0.09	0.09	0.15	0.07	0.12	0.08	0.10	0.00	0.01	0.04	0.02
Ce ₂ O ₃ (wt%)	0.00	0.25	0.19	0.19	0.04	0.01	0.18	0.00	0.00	0.09	0.07
MnO (wt%)				0.16			0.09			0.13	0.16
F (wt%)	0.44	1.01	1.34	1.37	2.56	3.15	3.34	2.81	2.35	3.09	3.00
Cl (wt%)	3.28	2.14	1.91	2.06	0.50	0.23	0.15	0.10	0.34	0.11	0.32
O = F, Cl	−0.92	−0.93	−1.00	−1.04	−1.18	−1.38	−1.44	−1.10	−1.47	−1.33	−1.33
Total (wt%)	99.77	100.32	100.95	99.79	99.69	100.23	99.95	100.73	100.62	100.32	99.88
P	5.882	5.790	5.931	5.975	5.870	5.934	5.941	5.902	5.834	5.977	5.792
Si	0.038	0.026	0.026	0.019	0.015	0.016	0.020	0.015	0.034	0.012	0.053
Fe	0.062	0.058	0.000	0.020	0.036	0.004	0.010	0.018	0.029	0.009	0.017
Mg	0.006	0.011	0.004	0.000	0.006	0.004	0.000	0.000	0.008	0.000	0.005
Ca	10.095	10.337	10.077	9.955	10.138	10.017	9.966	10.109	9.844	9.905	9.853
Na	0.009	0.002	0.003	0.007	0.027	0.026	0.029	0.022	0.125	0.030	0.121
S	0.006	0.005	0.003	0.000	0.026	0.026	0.024	0.022	0.124	0.025	0.148
Sr	0.012	0.000	0.000	0.000	0.009	0.007	0.016	0.009	0.022	0.015	0.019
Y	0.007	0.013	0.000	0.000	0.000	0.002	0.003	0.000	0.005	0.003	0.003
La	0.006	0.006	0.010	0.005	0.007	0.005	0.006	0.000	0.001	0.002	0.001
Ce	0.000	0.015	0.012	0.012	0.002	0.000	0.011	0.000	0.000	0.006	0.004
Mn				0.022			0.012			0.019	0.022
F	0.232	0.538	0.709	0.732	1.352	1.663	1.779	1.489	1.246	1.633	1.595
Cl	0.939	0.611	0.541	0.590	0.142	0.065	0.042	0.029	0.098	0.032	0.091
OH _{calc}	0.829	0.850	0.750	0.677	0.506	0.272	0.179	0.482	0.656	0.335	0.315
X _F	0.116	0.269	0.354	0.366	0.676	0.831	0.890	0.745	0.623	0.817	0.797
X _{Cl}	0.469	0.306	0.271	0.295	0.071	0.032	0.021	0.014	0.049	0.016	0.045
X _{OH}	0.415	0.425	0.375	0.339	0.253	0.136	0.089	0.241	0.328	0.168	0.157
S _{melt} (ppm, Parat11)					28	29	25	24	3991	27	13683
S _{melt} (ppm, Peng97)					138	140	124	118	656	131	785
K _d ^{ap-melt} _{Cl-OH} ^a	17.57	12.72	13.07		10.21	11.73		9.43	8.59		
Cl _{melt} (wt%) ^a	0.70	0.61	0.60		0.30	0.22		0.07	0.19		
K _d ^{ap-melt} _{Cl-OH} ^b	20.08	14.32	14.73		11.32	13.09		10.42	9.45		
Cl _{melt} (wt%) ^b	0.61	0.54	0.53		0.27	0.20		0.06	0.17		

^a Calculated according to Li and Hermann (2017) at 850 and 900 °C for the gabbrodiorite complex and porphyries, respectively^b Calculated according to Li and Hermann (2017) at 800 and 850 °C for the gabbrodiorite complex and porphyries, respectively

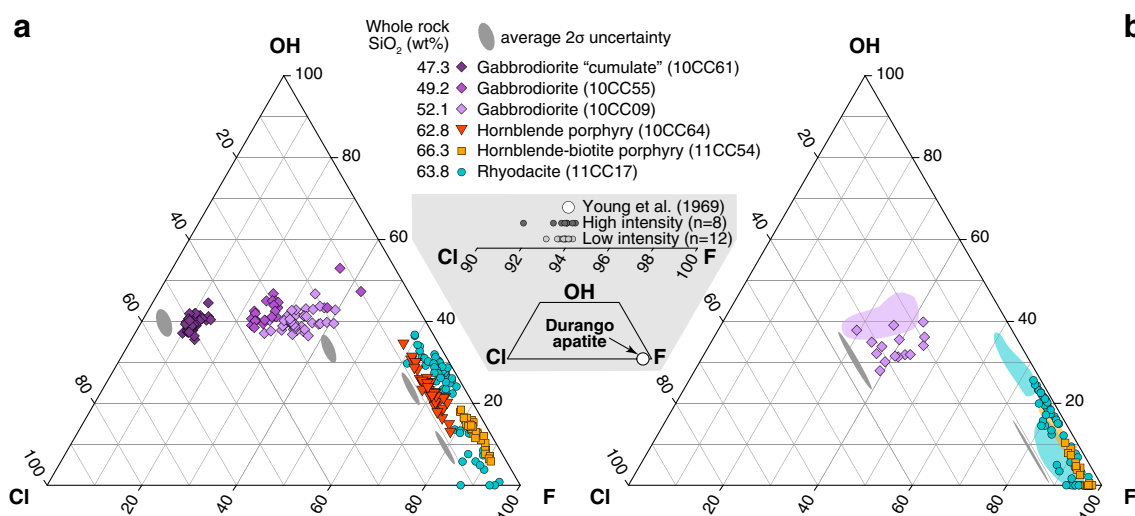


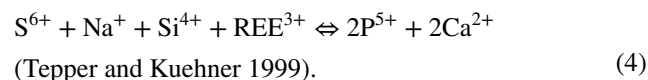
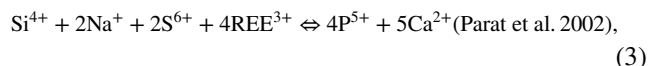
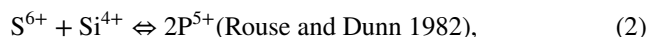
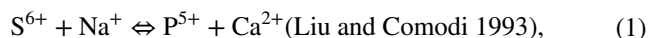
Fig. 3 Triangular plots of molar proportion of Cl, F and OH in the hydroxyl site of apatite from Corocochuayco, Peru. **a** Data acquired with the LI method. **b** Data acquired with the HI method. Colored fields in **b** show the contours of the results from the same apatite

in halogen concentration between apatite hosted in hornblende and apatite hosted in anhydrous phases (plagioclase, groundmass, quartz). Halogen contents from apatites of the gabbrodiorite complex and the porphyries plot in two markedly different fields (Fig. 3). There is also a general tendency of decreasing the molar Cl proportion of apatite with increasing host-rock silica content (Fig. 3). Apatite from the gabbrodiorite complex has constant molar OH proportion (~40%), while F concentration increases (from ~0.4 to ~1.2 wt%) and Cl concentration decreases (from ~3.4 to ~1.9 wt%, with only few outliers) from the least to the most siliceous sample. In the porphyries, apatite has an invariably low Cl concentration (<0.9 wt%) and falls along an F–OH exchange line. Apatite from the hornblende porphyry has Cl concentration of ~0.5 wt% and F concentration of 2.2–3.0 wt%. Apatite from the hornblende–biotite porphyry has lower Cl (~0.2 wt%) and higher F concentration (3.0–3.5 wt%). Finally, most analyses of apatite from the rhyodacite yield F concentration similar to those from the hornblende porphyry, but comparatively lower Cl concentration (~0.3 wt%). Few apatite grains from the rhyodacite define an F-rich group (fluorapatite proportion >80%).

Sulfur concentrations in apatite from the gabbrodiorite complex are always below 0.1 wt% SO₃ (i.e., <0.015 S pfu; Fig. 4a–d) and most of the time below the limit of detection. In contrast, apatite from the porphyries yield S concentrations that are always above this value, with a median of ~0.2 wt% SO₃ (~0.028 S pfu) for both the hornblende and hornblende–biotite porphyry, and of ~0.3 wt% SO₃ (~0.041 S pfu) for the rhyodacite (Fig. 4a–d). In the rhyodacite and, to a lesser extent, in the hornblende–biotite porphyry, few analyses have yielded high sulfur concentrations over 0.5

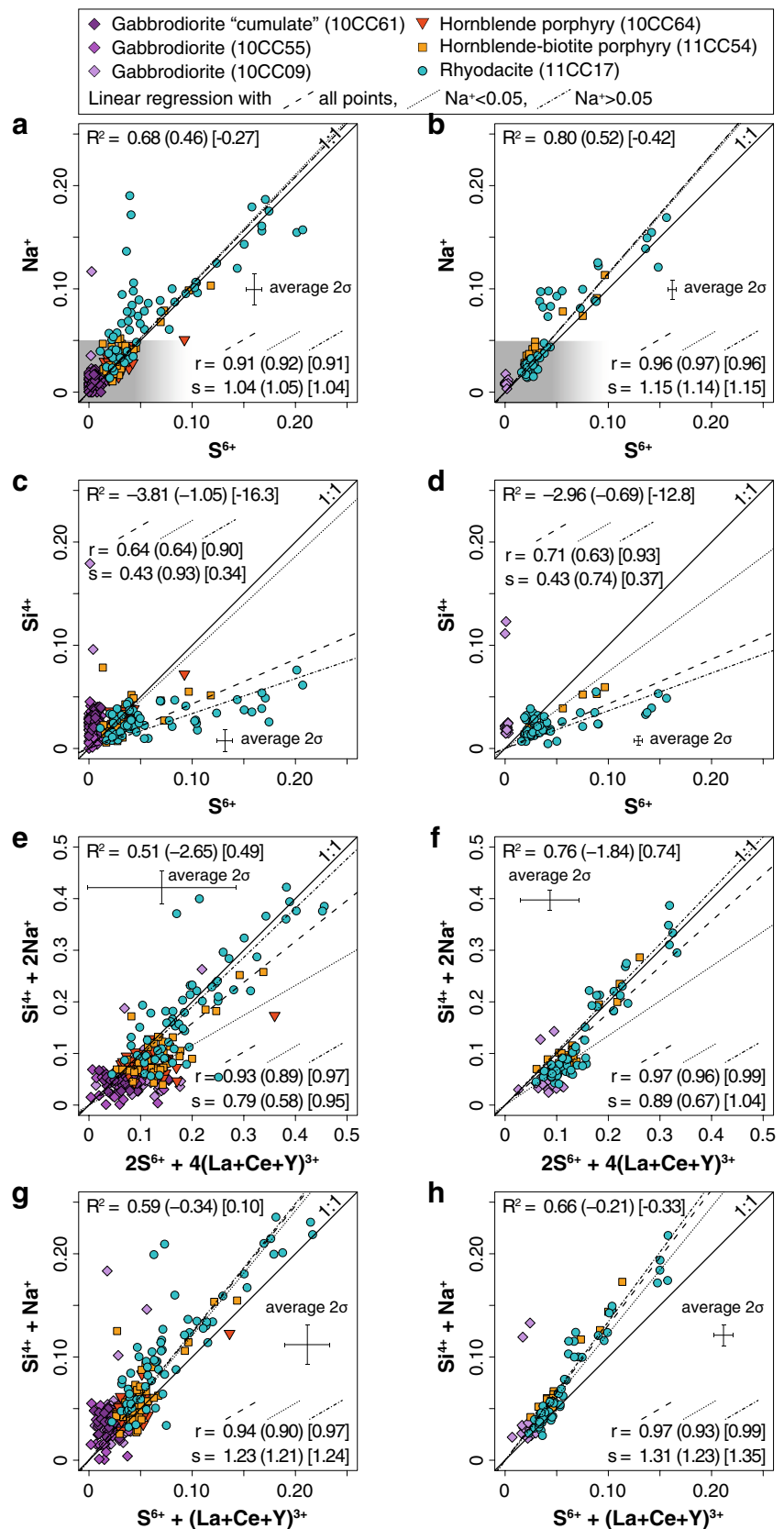
grains analyzed with the LI method. Inset with gray background shows the results from repeated measurements of the Durango apatite using both methods compared to the published values of Young et al. (1969)

wt% SO₃ and up to 1.6 wt% SO₃. Sulfur has been proposed to enter the apatite crystal structure mainly in the oxidized form S⁶⁺ by replacing P⁵⁺ through a charge-balanced coupled substitution possibly involving Na⁺, Si⁴⁺, REE³⁺ and Y³⁺ cations (Rouse and Dunn 1982; Liu and Comodi 1993; Tepper and Kuehner 1999; Parat et al. 2002). A recent S XANES study has shown that minor amounts of S⁴⁺ and S²⁻ can also enter the structure of apatite as a function of oxygen fugacity (Konecke et al. 2017). However, due to the expected low abundance of S⁴⁺ and S²⁻ in magmatic apatite (likely <<300 ppm), we will assume that all S we analyzed is in the form of S⁶⁺ ions. The possible exchange reactions are:



Among these, reaction (1) provides the best explanation for the compositional variability of apatite from Corocochuayco (Fig. 4). Indeed, Eq. (1), that is, a 1:1 relationship between S⁶⁺ and Na⁺, yields the best (closest to 1) coefficient of determination (R^2) for our data and a slope (s) closest to 1 for an origin-constrained linear regression through the data (LI: $R^2 = 0.68$, $s = 1.04$; HI: $R^2 = 0.80$, $s = 1.15$; Fig. 4a, b). However, a number of analyses, mainly from the rhyodacite, show high apatite Na⁺ content that cannot be explained by

Fig. 4 Possible sulfate exchange reactions for per formula unit cations and sulfur in apatite from Corocochuayco, Peru. Data in the left column (plots **a**, **c**, **e** and **g**) have been acquired with the LI method and data in the right column (plots **b**, **d**, **f** and **h**) with the HI method. R^2 coefficient of determination of a fixed 1:1 model (solid black line) for the data; r correlation coefficient of an origin-constrained linear regression through the data; s slope of this linear regression. Numbers in parentheses were calculated for a subset of the data having $\text{Na}^+ < 0.05$, corresponding to the gray field in **a** and **b**. Numbers in brackets were calculated for a subset of the data having $\text{Na}^+ > 0.05$. Dashed lines represent the origin-constrained linear regression through all the data. Negative coefficients of determination indicate that the 1:1 model provides a very poor description of the data



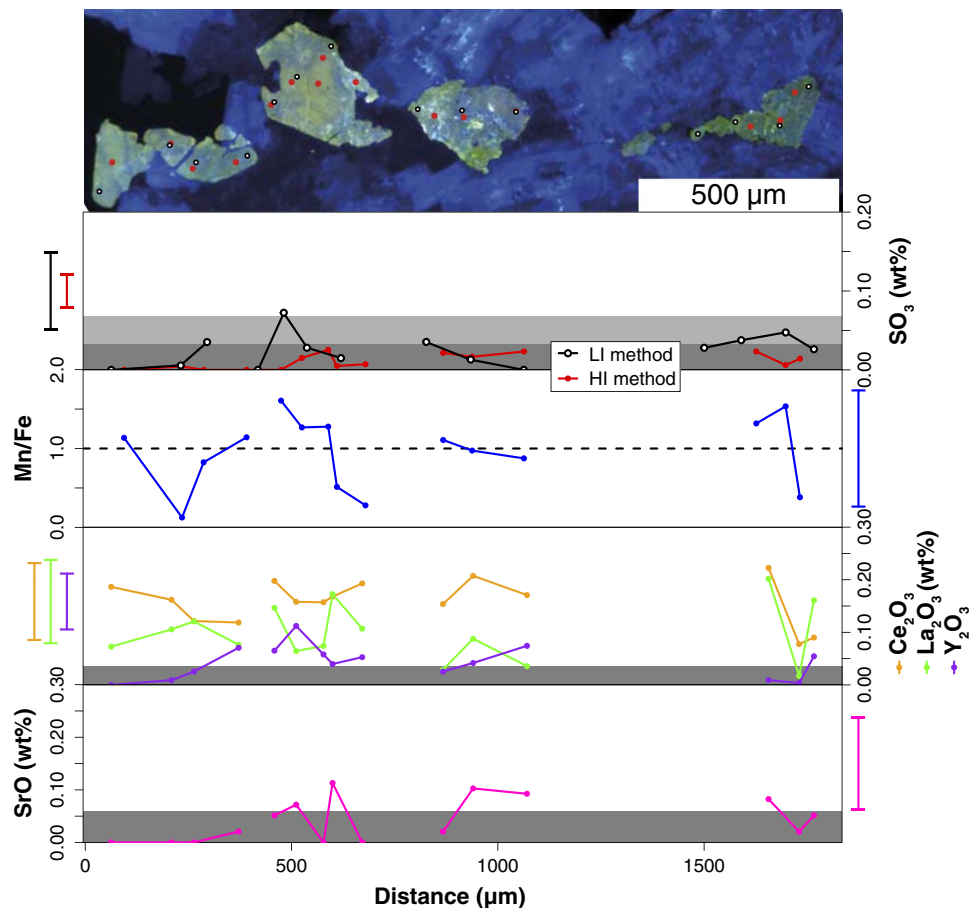
S^{6+} substitution alone (see apatite with $0.20 > Na^+ > 0.06$ pfu for $S^{6+} \sim 0.05$ pfu on Fig. 4a, b). When only points with $Na^+ > 0.05$ pfu are considered, reaction (3) yields the best statistics for our data (LI: $R^2 = 0.49$, $s = 0.95$; HI: $R^2 = 0.74$, $s = 1.04$; Fig. 4e, f). In turn, when only points with $Na^+ < 0.05$ pfu are considered, reaction (1) still yields the best statistics for our data (LI: $R^2 = 0.46$, $s = 1.05$; HI: $R^2 = 0.52$, $s = 1.14$; Fig. 4a, b).

Other trace elements (considering only the HI analyses) in apatite from Corocochuayco show less contrasted behavior between the gabbrodiorite and the porphyries, even though apatite CL images of porphyry apatites reveal more complex zoning than those in the gabbrodiorite (Figs. 5, 6, 7). The average FeO concentrations are similar in both groups (median at 0.08 wt%), while MnO concentrations are slightly lower in apatites from the gabbrodiorite compared to those in the porphyries (medians of 0.08 and 0.12 wt%, respectively) resulting in median Mn/Fe ratios of 1.1 and 1.4, respectively. Similarly, Sr was more often below detection limit in apatites from the gabbrodiorite than in those of the porphyries. In turn, REE₂O₃ (La, Ce and Y) are on average slightly more concentrated in apatite from the gabbrodiorite with respect to those from the porphyries (median La₂O₃ = 0.09 wt%, Ce₂O₃ = 0.16 wt% and Y₂O₃ = 0.04

wt% for the gabbrodiorite and median La₂O₃ = 0.07 wt%, Ce₂O₃ = 0.13 wt% and Y₂O₃ = 0.03 wt% for the porphyries).

In detail, microprobe profiles through apatite show little chemical zoning in grains from the gabbrodiorite and the hornblende–biotite porphyry, consistent with the limited zoning observed on CL images (all values overlap within analytical error; Figs. 5, 6). Instead, subhedral to anhedral grains with patchy CL textures in both rock units show noisy chemical patterns (Figs. 5, 6a). Nevertheless, profiles on apatite from the rhyodacite reveal much more complex zoning patterns (Fig. 7). In the rhyodacite, apatite grains that show concentric CL zoning have chemistries comparable to apatite from the hornblende–biotite porphyry (of both the patchy and concentric zoning types; Figs. 6, 7a). The blue cores are slightly enriched in SO₃ (up to 0.4 wt%) and to a lesser extent in REEs compared to the blue-green overgrowth (although mostly overlapping within uncertainty). In turn, apatite grains from the rhyodacite that show dissolution/overgrowth textures on CL images return the highest sulfur concentrations (> 0.5 wt% SO₃) and display complex zoning with no consistency from one grain to another (even for grains in contact; Fig. 7b, c). For example, the biggest apatite on Fig. 7b has a S-rich rim, while the smaller grain has an S-rich core. In both cases, this S-rich domain

Fig. 5 CL image and chemical composition of apatite grains within the gabbrodiorite (sample 10CC09). Gray fields correspond to the average limit of detection of the LI (light gray) and HI (dark gray) methods for the corresponding trace element. The error bars on the side of each plot correspond to the average 2σ analytical uncertainty of the corresponding compound or ratio



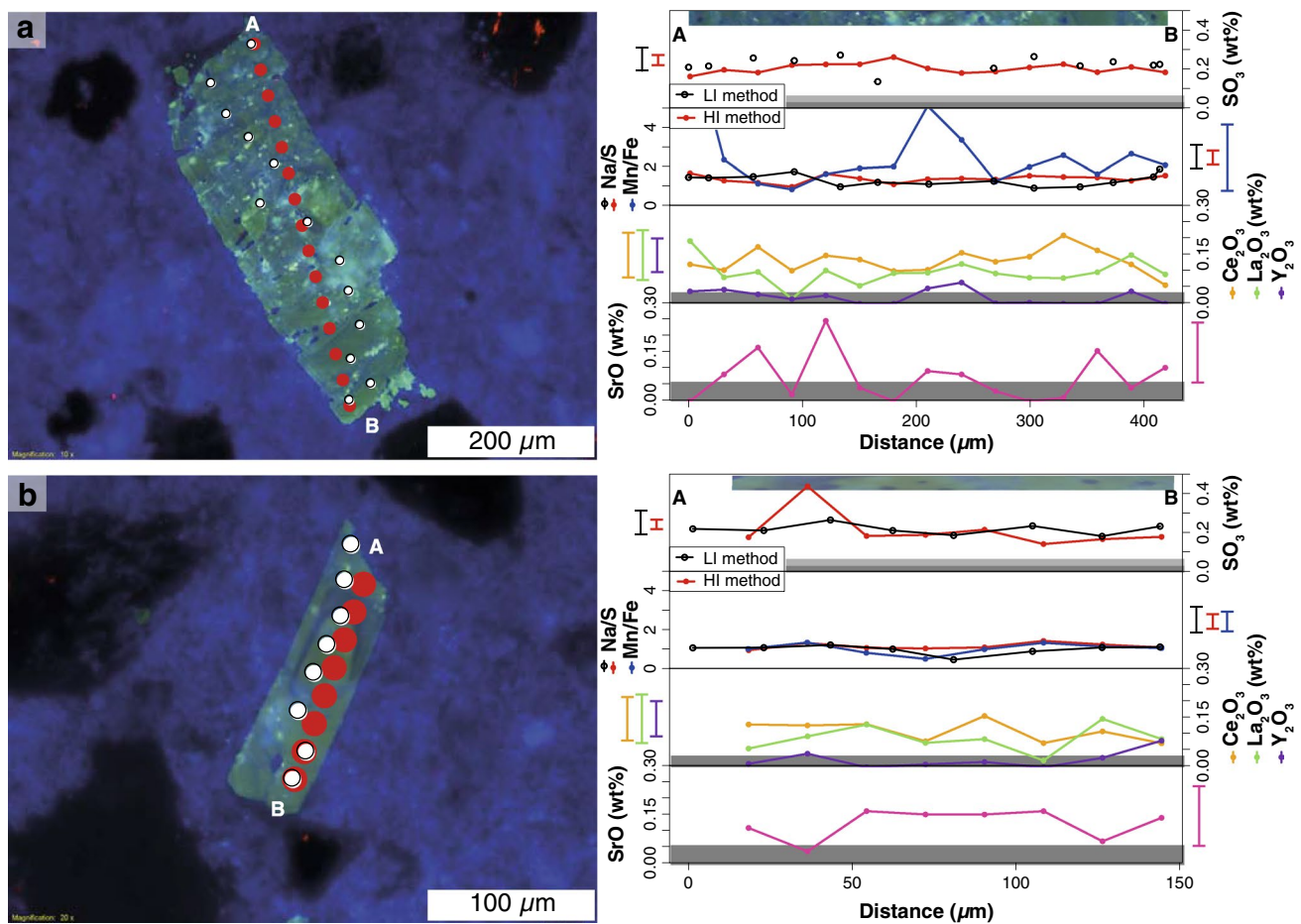


Fig. 6 CL image and chemical compositional profiles on apatite grains within the hornblende–biotite porphyry (sample 11CC54). Gray fields correspond to the average limit of detection of the LI (light gray) and HI (dark gray) methods for the corresponding trace

corresponds to darker and bluer CL response as well as higher Sr concentrations (> 0.20 wt% SrO). However, in the bigger grain, the blue-green core, which has SO_3 concentration around 0.2 wt%, is also anomalously enriched in Na ($\text{Na/S} > 2$) and Y ($\text{Y}_2\text{O}_3 > 0.15$ wt%; but not in La and Ce), features which are not observed in the smaller grain. In apatite grains shown in Fig. 7c, the high S concentrations again correspond to CL darker and bluer domains. These domains also have low Mn/Fe ratios (< 0.8) and Na/S ratios around 1. In turn the CL greener domains have comparatively lower S concentrations, $\text{Na/S} \sim 2$ and $\text{Mn/Fe} \sim 1$. REE are low (< 0.15 wt% REE_2O_3) and essentially overlapping within uncertainty across the different CL zones (Fig. 7c).

Amphibole

Amphibole chemical data are taken from Chelle-Michou et al. (2015a; see representative amphibole compositions Table 2) and include 235 analyses from all rock units at

Corocohuayco (including 107 from the gabbrodiorite complex and 128 from the porphyries) with the exception of the rhyodacite where no unaltered amphibole could be found. Amphibole formulae were calculated on the basis of a 13-cation normalization following the guidelines of Giesting and Filiberto (2014). According to the classification of Leake et al. (1997), most amphiboles from Corocohuayco are magnesio-hornblende (58%) and a lesser proportion are edenite (19%; only in the porphyries), tschermakite (13%; only in the gabbrodiorite complex) and magnesio-hastingsite (11%).

In both rock units, Al_{tot} mostly varies from 2.0 to 0.8 pfu, and a distinct group of high-Al amphibole (Al_{tot} from 1.8 to 2.4 pfu) is also present in the porphyries (Fig. 8). Variations in Al_{tot} are mostly accounted for by the edenite exchange reaction, while the Al-tschermak substitution plays only a minimal role in these variations (Fig. 8a, b). In contrast, for the high-Al amphiboles, variations of Al_{tot} are strongly

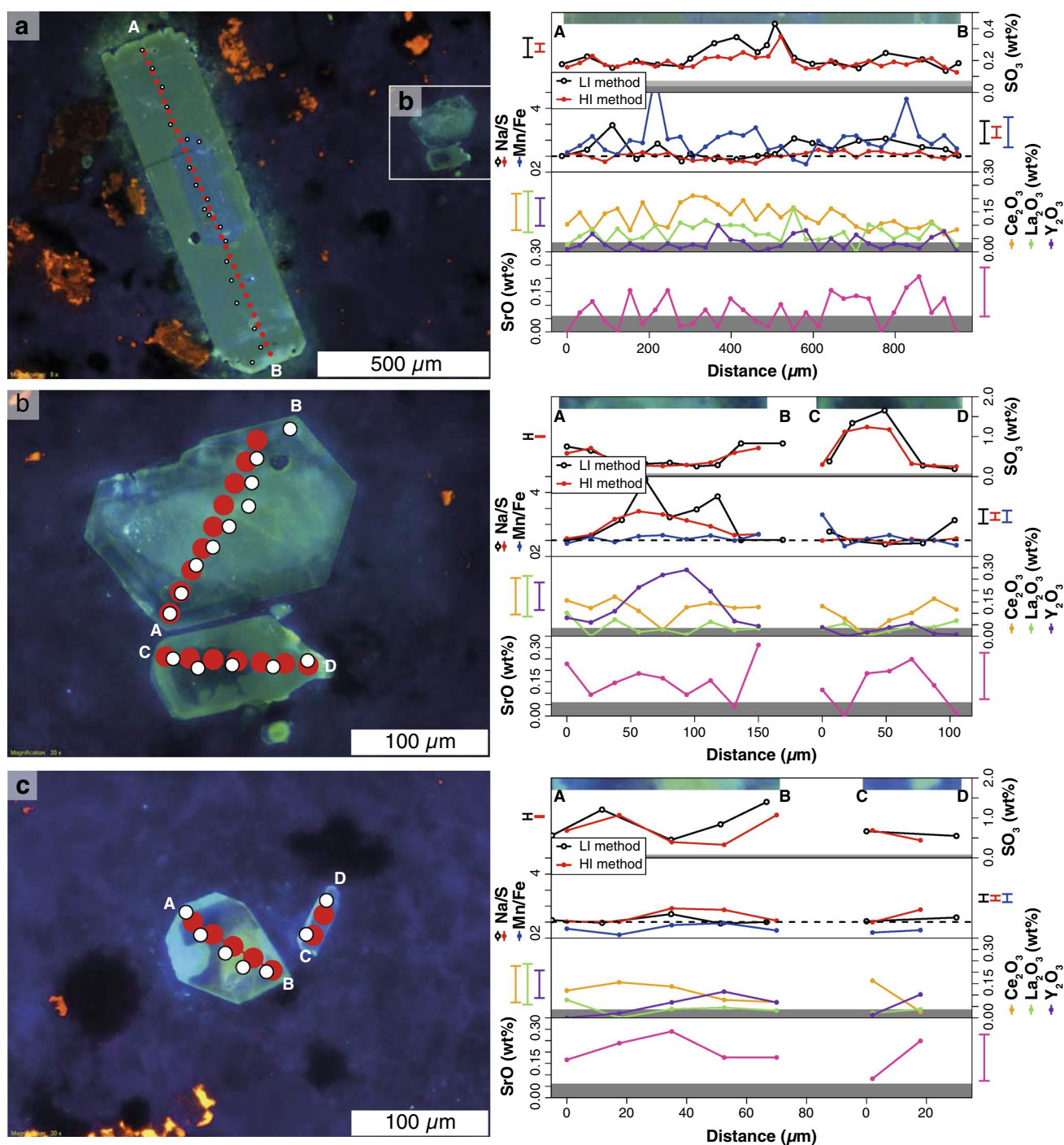


Fig. 7 CL image and chemical compositional profiles on apatite grains within the rhyodacite (sample 11CC17). Gray fields correspond to the average limit of detection of the LI (light gray) and HI

(dark gray) methods for the corresponding trace element. The error bars on the side of each plot correspond to the average 2σ analytical uncertainty of the corresponding compound or ratio

controlled by the Al-tschermak substitution rather than by the edenite substitution.

In the gabbrodiorite complex, amphibole Cl contents are scattered and vary from ca. 0.1 to 0.4 wt% (0.02–0.08 pfu; Fig. 8c). In detail, amphibole with $Al_{tot} > 1.8$ pfu and $Al_{tot} < 1.1$ pfu (mostly from the ‘gabbrodiorite cumulate’)

tend to have a more restricted and low Cl concentration of 0.01–0.04 pfu. In turn, the most scattered Cl concentrations (0.02–0.08 pfu) correspond to Al_{tot} of 1.2–1.6 pfu. Amphiboles from the porphyries generally show lower and more restricted Cl concentrations of 0.04–0.13 wt% (ca.

Table 2 Representative amphibole composition from the Corocohuayco magmatic suite. Data from Chelle-Michou et al. (2015a)

Unit	Gabbrodiorite “cumulate”				Gabbrodiorite				Hornblende porphyry				Hornblende–biotite porphyry			
	10CC61	10CC101	10CC101	ampD8	10CC09	10CC09	10CC09	ampE5	10CC55	10CC64	10CC64	10CC64	10CC34	10CC34	10CC34	10CC34
Sample	ampD1	ampA4	ampD8	ampD8	ampA4	ampD3	ampE5	ampC2	ampA4	ampC1	ampE5	ampG4	ampH4	ampL6	ampL9	ampH41
SiO ₂ (wt%)	47.75	45.10	42.57	44.55	44.55	45.24	46.79	44.42	45.87	45.74	43.79	47.33	47.10	46.70	48.63	45.17
TiO ₂ (wt%)	1.78	2.07	3.04	2.34	2.34	2.19	1.34	2.39	1.82	1.37	1.70	1.37	1.35	1.39	1.01	1.53
Al ₂ O ₃ (wt%)	7.00	9.00	11.01	9.23	9.23	8.96	6.96	9.54	8.01	8.73	9.18	7.51	7.27	7.48	5.96	8.30
Cr ₂ O ₃ (wt%)	0.00	0.00	0.01	0.02	0.02	0.02	0.00	0.00	0.00	0.04	0.02	0.00	0.00	0.02	0.00	0.04
FeO _{tot} (wt%)	14.40	16.06	13.52	14.85	14.85	15.06	16.41	13.12	14.71	16.26	16.51	15.22	14.71	15.01	13.80	15.26
MnO (wt%)	0.31	0.28	0.20	0.31	0.31	0.32	0.48	0.29	0.52	0.53	0.52	0.51	0.57	0.56	0.54	0.56
MgO (wt%)	14.25	11.96	12.71	12.93	12.93	12.54	12.70	13.79	12.83	11.62	11.47	12.67	13.01	12.90	14.21	12.35
CaO (wt%)	11.04	10.91	10.67	11.17	11.17	11.27	10.84	11.30	11.23	11.25	11.05	11.36	11.53	11.41	11.67	11.40
Na ₂ O (wt%)	1.23	2.11	2.51	1.66	1.66	1.65	1.23	1.89	1.95	1.94	2.17	1.75	1.98	2.04	1.68	2.17
K ₂ O (wt%)	0.22	0.66	0.47	0.48	0.48	0.46	0.36	0.35	0.80	0.91	0.97	0.73	0.70	0.71	0.60	0.88
F (wt%)	0.00	0.00	0.00	0.00	0.00	0.00	0.00	0.00	0.00	0.00	0.00	0.00	0.00	0.00	0.00	0.00
Cl (wt%)	0.12	0.24	0.09	0.20	0.20	0.21	0.22	0.12	0.06	0.08	0.09	0.07	0.05	0.05	0.04	0.06
O = F, Cl (wt%)	−0.03	−0.05	−0.02	−0.04	−0.04	−0.05	−0.05	−0.03	−0.01	−0.02	−0.02	−0.02	−0.01	−0.01	−0.01	−0.01
Total (wt%)	98.07	98.35	96.78	97.69	97.69	97.88	97.28	97.18	97.78	98.45	97.44	98.50	98.26	98.27	98.13	97.70
^{IV} Si	6.830	6.605	6.270	6.496	6.496	6.606	6.830	6.471	6.735	6.722	6.525	6.893	6.890	6.833	7.056	6.689
^{IV} Al	1.170	1.395	1.730	1.504	1.504	1.394	1.170	1.529	1.265	1.278	1.475	1.107	1.110	1.167	0.944	1.311
^{IV} Ti	0.000	0.000	0.000	0.000	0.000	0.000	0.000	0.000	0.000	0.000	0.000	0.000	0.000	0.000	0.000	0.000
^{IV} Al	0.010	0.158	0.181	0.082	0.082	0.148	0.027	0.109	0.121	0.234	0.137	0.182	0.143	0.123	0.075	0.138
^{IV} Ti	0.191	0.228	0.337	0.257	0.257	0.240	0.147	0.262	0.201	0.151	0.190	0.150	0.149	0.153	0.110	0.170
^{IV} Cr	0.000	0.000	0.001	0.002	0.002	0.002	0.000	0.000	0.000	0.004	0.002	0.000	0.000	0.003	0.000	0.005
^{IV} Fe ³⁺	1.014	0.634	0.702	0.859	0.859	0.682	1.043	0.769	0.505	0.471	0.616	0.450	0.363	0.445	0.437	0.422
^{IV} Mg	3.039	2.611	2.791	2.810	2.810	2.730	2.763	2.995	2.808	2.546	2.548	2.751	2.837	2.814	3.074	2.727
^{IV} Fe ²⁺	0.709	1.333	0.964	0.952	0.952	1.158	0.960	0.829	1.302	1.528	1.441	1.404	1.437	1.392	1.237	1.468
^{IV} Mn	0.038	0.035	0.025	0.039	0.039	0.039	0.059	0.036	0.064	0.066	0.065	0.063	0.071	0.070	0.067	0.071
^{IV} Fe ²⁺	0.000	0.000	0.000	0.000	0.000	0.000	0.000	0.000	0.000	0.000	0.000	0.000	0.000	0.000	0.000	0.000
^{IV} Ca	1.692	1.712	1.684	1.745	1.745	1.763	1.695	1.764	1.767	1.771	1.764	1.773	1.807	1.789	1.814	1.809
^{IV} Na	0.308	0.288	0.316	0.255	0.255	0.237	0.305	0.236	0.233	0.229	0.236	0.227	0.193	0.211	0.186	0.191
^{IV} Na	0.032	0.311	0.401	0.214	0.214	0.230	0.043	0.298	0.322	0.324	0.391	0.267	0.369	0.368	0.287	0.432
^{IV} K	0.040	0.124	0.089	0.090	0.090	0.086	0.067	0.065	0.150	0.171	0.184	0.135	0.131	0.133	0.110	0.166
F	0.000	0.000	0.000	0.000	0.000	0.000	0.000	0.000	0.00	0.00	0.00	0.00	0.00	0.00	0.00	0.00
Cl	0.029	0.059	0.023	0.048	0.048	0.053	0.053	0.030	0.015	0.019	0.022	0.017	0.012	0.013	0.011	0.015
OH _{calc}	1.971	1.941	1.977	1.952	1.952	1.947	1.947	1.970	1.98	1.98	1.98	1.98	1.99	1.99	1.99	1.98
P (MPa) ^a	120	169	295	193	193	176	118	210	148	220	289	126	120	176	91	238
T (°C) ^a	786	847	949	857	857	832	785	881	858	849	896	808	832	854	790	885

Table 2 (continued)

Unit	Gabbrodiorite "cumulate"				Gabbrodiorite				Hornblende porphyry				Hornblende-biotite porphyry			
Sample	10CC61	10CC101	10CC101	10CC101	10CC09	10CC09	10CC09	10CC09	10CC64	10CC64	10CC64	10CC64	10CC34	10CC34	10CC34	10CC34
Spot	ampD1	ampA4	ampD8	ampD8	ampA4	ampA4	ampD3	ampE5	ampA4	ampC1	ampE5	ampG4	ampH4	ampL6	ampL9	ampHA1
ΔNNO^a	-1.0	0.5	0.6	0.6	-0.3	-0.3	-0.4	-0.7	1.9	2.0	2.3	1.5	2.2	2.2	2.1	2.8
$\text{H}_2\text{O}_{\text{melt}}^a$	5.2	5.0	4.5	4.5	5.3	5.3	5.6	5.4	4.5	6.1	5.9	5.1	4.6	5.2	4.7	5.6
$K_{\text{Cl-OH}}^{\text{amp-melt},b}$	0.361	0.892	0.545	0.545	0.595	0.595	0.629	0.582	0.892	1.359	1.527	0.859	0.787	0.815	0.552	1.143
$\text{Cl}_{\text{melt}} (\text{wt}\%)^b$	0.34	0.29	0.18	0.18	0.37	0.37	0.39	0.40	0.09	0.09	0.10	0.12	0.08	0.10	0.11	0.08

^aCalculated according to Ridolfi and Renzulli (2012)^bCalculated according to Giessing and Filiberto (2014)

0.01–0.03 pfu) which positively correlate with Al_{tot} , except for the high-Al group (Fig. 8c).

Profiles through amphibole crystals (Fig. 9) reveal that (1) temperature-sensitive elements (Al, $^{\text{A}}[\text{Na} + \text{K}]$ and Ti) can vary greatly within a single crystal with no regular core–rim trend, but that high values correspond to brighter zones in BSE images, (2) crystal-scale Cl variations are much more subtle, but correlate with temperature-sensitive elements (see also Fig. 8c) and (3) the variability of these elements in amphibole is smaller in single crystals than at the scale of the sample.

Crystallization conditions of minerals

Amphibole

Intensive parameters (P , T , $f\text{O}_2$, $\text{H}_2\text{O}_{\text{melt}}$) at the time of amphibole crystallization were estimated based on amphibole composition (Chelle-Michou et al. 2015a) using the empirical formulations of Ridolfi and Renzulli (2012). Despite having distinct compositions (probably reflecting different magma compositions; Fig. 8; Table 2), amphiboles from both the gabbrodiorite complex and the porphyries record similar pressure, temperature and melt water content estimates of 250–100 MPa, 900–750 °C and 5 ± 1 wt%, respectively. Oxygen fugacities obtained from amphibole of the gabbrodiorite complex were $\text{NNO} \pm 1$ (where NNO is the Ni–NiO oxygen buffer) and from $\text{NNO} + 1$ to $\text{NNO} + 2$ for the porphyries. Despite debates on the accuracy of the calculated parameters using these empirical calibrations (e.g., Walker et al. 2013; Erdmann et al. 2014), Chelle-Michou et al. (2015a) used independent mineralogical, chemical and thermodynamic constraints to argue that they represent overall reasonable estimates of intensive parameters for the magmas in equilibrium with amphibole at Corocohuayco (see below). Importantly, the predominance of the edenite exchange reaction in amphibole from Corocohuayco supports the temperature-controlled compositional variations with minimal influence from pressure variations (Fig. 8a, b).

To test the accuracy of the estimated pressure and temperature as determined by the empirical formulation of Ridolfi and Renzulli, Chelle-Michou et al. (2015a) used these P – T estimates to calculate the composition of plagioclase that would theoretically be in equilibrium with amphibole using the thermodynamic amphibole–plagioclase thermobarometer of Holland and Blundy (1994). For the gabbrodiorite complex, the estimated plagioclase composition always remarkably matches the measured composition of the plagioclase rims within each sample, which is consistent with the poikilitic texture of amphibole in these samples. In turn, estimated plagioclase composition for the porphyries was always higher than the measured one (estimated An30–60 vs

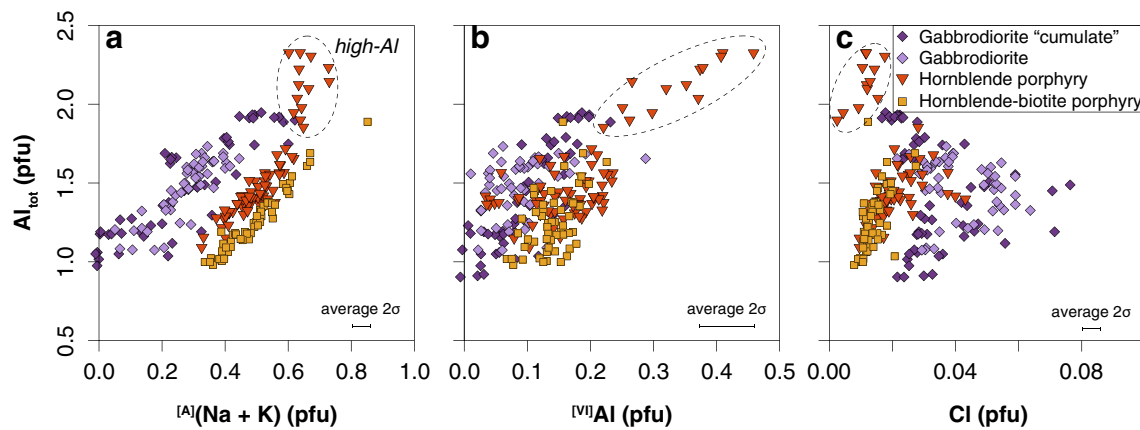


Fig. 8 Amphibole composition in per formula unit. **a** Edenite exchange. **b** Al-tschermak exchange. **c** Cl vs Al_{tot} . Data are from Chelle-Michou et al. (2015a)

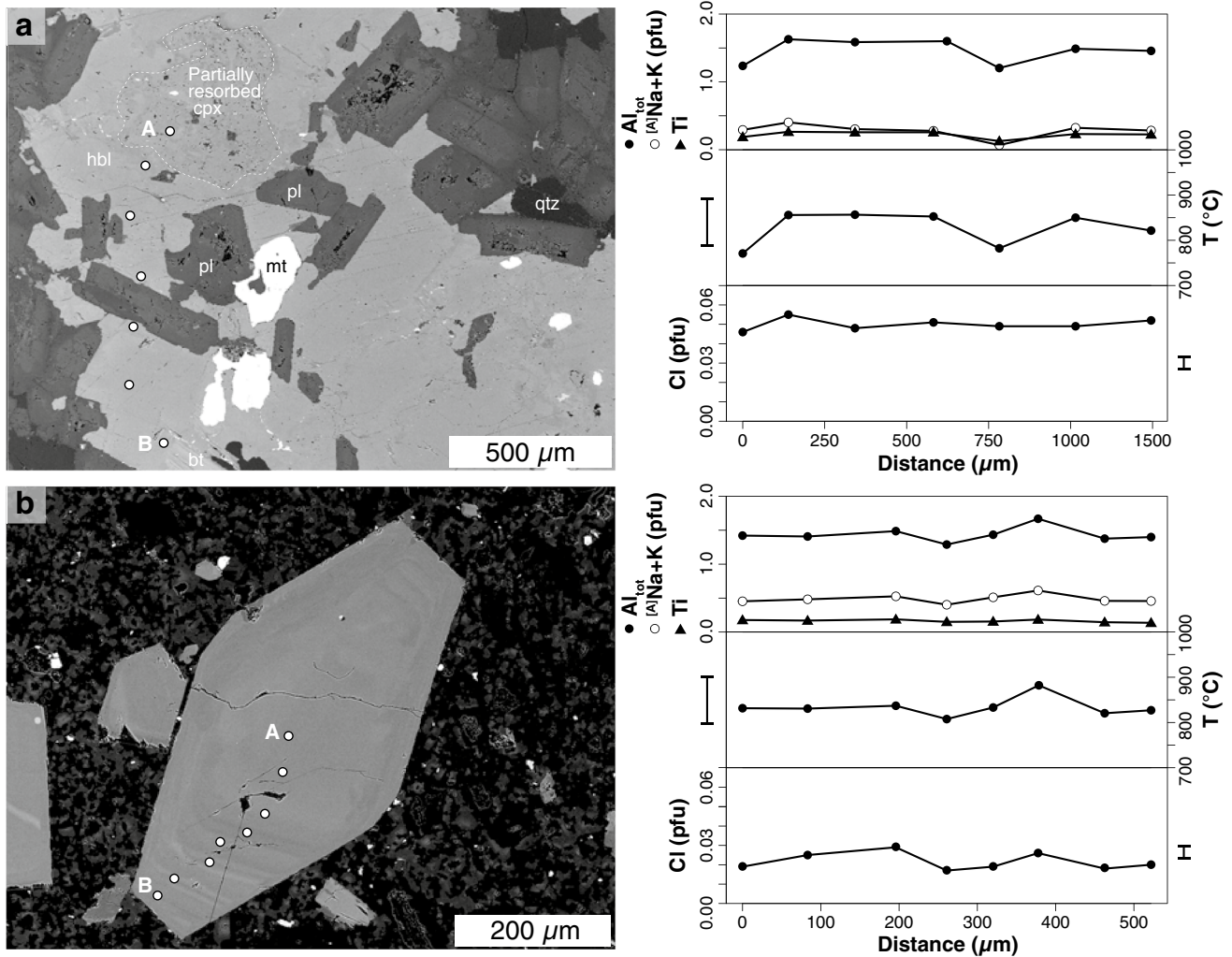


Fig. 9 BSE image and chemical compositional profiles on amphibole crystals within **a** the gabbrodiorite and **b** the hornblende porphyry. The error bar for the Cl plot corresponds to the average 2σ analytical uncertainty and that for the temperature plot is that the thermometer

uncertainty of ± 24 °C (see Ridolfi and Renzulli 2012). Analytical uncertainty for the temperature-sensitive elements (Al_{tot} , $[A](Na + K)$ and Ti) is smaller than the size of the symbol. Data are from Chelle-Michou et al. (2015a)

measured An10–30, respectively). However, using the measured plagioclase and amphibole compositions with the thermobarometric formulation of Holland and Blundy (1994) in conjunction with the Al-in-hornblende barometer of Anderson and Smith (1995) resulted in a restricted near-solidus temperature range around 700 °C and a large pressure range of 400–100 MPa (Chelle-Michou et al. 2015). This is inconsistent with the well-developed edenite exchange vector and the lack of tschermak exchange in amphibole from Corocohuayco (Fig. 8a, b). This is also inconsistent with the crystallinity of the porphyries (~ 50% crystals, ~ 50% groundmass) showing that the dacitic magma was at ca. 800–850 °C at the time of porphyry emplacement. These observations suggest that the pressure and temperature estimates using the empirical formulation of Ridolfi and Renzulli (2012) represent reasonable values for the porphyries. The increase in oxygen fugacity from the gabbrodiorite complex to the porphyries is supported by a mineralogical change of the Ti phase from ilmenite to titanite and by the increasing zircon Ce anomaly (Chelle-Michou et al. 2014, 2015a). Finally, the estimated melt H₂O concentration is consistent with the facts that basic to silicic arc magmas are hydrous and that magmatic water saturation at 250–100 MPa is around 6–4 wt% (e.g., Baker and Alletti 2012). The observations that (1) magma crystallinity at the time of amphibole saturation in the gabbrodiorite was around 50–60 vol% (ca. 60 vol% plagioclase with 30 vol% of interstitial amphibole; Chelle-Michou et al. 2015a) and that (2) the porphyries are representative of an ore-forming magmatic–hydrothermal system further support that the magma was fluid saturated at the time of amphibole crystallization throughout the Corocohuayco magmatic suite (gabbrodiorite complex and porphyries). It is worth mentioning that the bulk of the crystal cargo of the porphyries (including plagioclase, amphibole and apatite) likely formed in an upper crustal magmatic system emplaced at 100–250 MPa and that magma was subsequently transferred to higher crustal levels (in stocks and dikes) at the time of mineralization (at around 25 MPa according to Maher 2010) where rapid cooling caused the porphyritic texture.

Calculations for the high-Al amphiboles from the porphyries result in higher pressures (500–1600 MPa), temperatures (900–1000 °C) and H₂O_{melt} (7–12 wt%; Chelle-Michou et al. 2015a). However, due to the lack of external constraints for these amphiboles, the robustness and accuracy of these intensive parameters should be taken with much caution. We can only mention that the predominance of the Al-tschermak substitution in these amphiboles and their high Al_{tot} (1.8–2.4 apfu) support their pressure-controlled compositional variations and that they crystallized at mid- to lower crustal depth. However, these amphibole crystals may have been sampled from deep crustal proto-plutons and would not bear information on the magma from which the porphyries crystallized.

Due to intra-crystal chemical variations in amphibole (Fig. 9), the estimated temperature record within a single crystal can vary up to 150 °C (70 °C on average). While the small intra-crystal variations (< 70 °C) may be explained by the uncertainty associated with the calibration of thermometer (± 24 °C, 1 σ ; Ridolfi and Renzulli 2012), larger variations likely record some temperature fluctuations during mineral crystallization.

Apatite

In the gabbrodiorite complex, euhedral to subhedral apatite is usually found enclosed in hornblende oikocrysts (enclosing euhedral plagioclase, Fig. 2b), while anhedral grains tend to fill the space between euhedral plagioclase crystals (Fig. 2a). It is noteworthy that subhedral and anhedral apatite grains have similar compositions. These features suggest that apatite co-crystallized with hornblende. Therefore, similar crystallization conditions (100–250 MPa, 750–900 °C, fO_2 of NNO ± 1 and fluid saturated) may be postulated for apatite in the gabbrodiorite complex. This temperature range can be confirmed by calculating the apatite saturation temperature (AST) for the estimated liquid composition at the time of apatite saturation (Harrison and Watson 1984), that is, the time of hornblende saturation (from petrographic observations). Based on the whole-rock composition (Supplementary Material 3), we recalculated the composition of the liquid by assuming that the magma was 50–60% crystalline with a mineral assemblage consisting of 88% of plagioclase (with an average An60–70 composition), 8% of magnetite, 2% of clinopyroxene (diopside) and 2% of high-temperature hornblende (> 900 °C) as suggested by petrographic observations, modal mineralogy and mineral chemistry (Chelle-Michou et al. 2015a). This approach is justified by the observation that the ca. 31 vol% of hornblende present in the gabbrodiorite is poikilitic and encloses plagioclase (63 vol%, An90–An30), resorbed clinopyroxene (0.5 vol%) and Fe–Ti oxides (5 vol%; Chelle-Michou et al. 2015a). This results in AST in the range of 800–870 °C, consistent with hornblende thermometry.

In the porphyries, apatite occurs as inclusions in all mineral phases and in the groundmass, and displays euhedral to subhedral habitus (Fig. 2c, d). This suggests that apatite crystallized close to the liquidus in these rocks. Assuming that the whole-rock chemistry approximates the composition of the liquid at the time of apatite crystallization, we calculate AST (Harrison and Watson 1984) in the range of 895–915 °C (Supplementary Material 3). These temperatures are indeed close to the water-saturated liquidus of dacitic magmas in the upper crust (900–950 °C; Scaillet and Evans 1999; Blundy and Cashman 2001; Costa et al. 2004). This is also similar to the highest crystallization temperature recorded by some low-Al amphibole (those with

$Al_{tot} \sim 1.6$ pfu) in the porphyries which are around 900 °C (see Chelle-Michou et al. 2015a).

Some apatites from the rhyodacite show dissolution/overgrowth textures (Fig. 7b). This is consistent with previous results showing that this rock was emplaced as a result of proto-pluton remelting under near-zircon saturated conditions (this rock contains mostly antecrystic zircon and very little autocrystic ones; Chelle-Michou et al. 2014). Chelle-Michou et al. (2014) proposed that this remelting event was the consequence of the establishment of a long-lived and large thermal anomaly in the crust culminating with the emplacement of a large volume dacitic magma that sourced the ore-forming fluids of the Corocohuayco deposit. Under these conditions, melting of a calc-alkaline proto-pluton or of the surrounding crust (sediments, volcanic rocks, older pluton) would have produced a peraluminous interstitial liquid ($A/CNK > 1$, where A/CNK is the $Al_2O_3/[CaO + Na_2O + K_2O]$ molar ratio) (Patiño Douce 1997). Such melt composition has been shown to dramatically increase apatite solubility compared to metaluminous melts with similar SiO_2 and P_2O_5 concentrations (Pichavant et al. 1992). This may provide an explanation for the dissolution textures observed in some apatite grains from the rhyodacite. Grains that lack dissolution/overgrowth textures and instead show concentric zoning are likely crystallized from a newly intruded dacitic magma. The slightly contrasted trace element composition of grains with dissolution/overgrowth textures (high $SO_3 > 0.5$ wt% and locally high $Y_2O_3 > 0.10$ wt%) and concentrically zoned grains ($SO_3 \sim 0.2$ wt% and $Y_2O_3 < 0.10$ wt%) could also be consistent with this hypothesis. Yet, in the absence of more precise analyses including an extended suite of trace elements (e.g., other REEs, U, Th, etc.) or of direct evidence for a peraluminous melt, this hypothesis cannot be tested further.

Sulfur concentration of the melt

Arc basalts typically contain hundreds to thousands ppm of dissolved sulfur (e.g., Wallace 2005; Wallace and Edmonds 2011) and the basaltic melt at the source of the gabbrodiorite complex probably had comparable S concentrations. Yet, the limited occasional presence of magmatic sulfide in the gabbrodiorite suggests that the melt was on the low side of that expected for arc basalts (probably within 300–1000 ppm). Apatite from the gabbrodiorite complex systematically returns very low sulfur concentrations (< 0.1 wt% SO_3). These low values may either (1) reflect low magmatic sulfur content of the basaltic magma or (2) fO_2 conditions at which the dominant sulfur specie is S^{2-} (Jugo et al. 2010; Baker and Moretti 2011) and thus cannot enter the apatite structure in high amounts (Parat et al. 2011b; Konecke et al. 2017). At the time of apatite saturation (> 850 °C), the interstitial melt likely was fluid saturated and a fraction of the sulfur would

have partitioned into the degassing magmatic fluid. Fluid/melt partition coefficients for sulfur in basaltic to andesitic melts at around NNO range from 1 to ca. 800 [see compilation in Webster and Botcharnikov (2011); corresponding to bulk S partition coefficient from 0.05 to 40 assuming 5 wt% H_2O in the melt] such that the sulfur concentration in the interstitial fluid-saturated melt may have increased or decreased upon fluid saturation and crystallization. Therefore, the melt sulfur concentration at apatite saturation in the gabbrodiorite complex remains unknown and the hypothesis that low S concentration in apatite could reflect low melt S concentration cannot be tested. On the other hand, the oxidation state of a silicic melt exerts a first-order control on sulfur speciation: from FMQ (where FMQ is the fayalite–magnetite–quartz oxygen buffer; ca. NNO-0.7) to FMQ + 2 (ca. NNO + 1.3) the dominant sulfur species rapidly changes from S^{2-} to S^{6+} (Jugo et al. 2010; Botcharnikov et al. 2011). Therefore, the low S content of apatite of the gabbrodiorite complex is also consistent with previous work showing that it corresponds to a magma in which S occurred mostly in its reduced form at NNO ± 1 (Chelle-Michou et al. 2014, 2015a).

In contrast, moderate (~ 0.2 wt% SO_3) to high (> 0.5 wt% SO_3) sulfur concentrations are recorded in apatite from the porphyries. These values are consistent with the higher oxidation state of the associated magma (NNO + 1 to NNO + 2; Chelle-Michou et al. 2014, 2015a). Using a set of natural and experimental apatite/melt partitioning data for andesitic to rhyolitic melts, Parat et al. (2011b) calibrated the following empirical non-Henrian partitioning relationship for sulfur between apatite and melt:

$$S_{\text{apatite}}(\text{wt}\%) = 0.0629 \times \ln S_{\text{melt}}(\text{wt}\%) + 0.4513. \quad (5)$$

This equation is constrained up to 0.1 wt% S in the melt (ca. 0.3 wt% S in apatite). When applied to apatite from the porphyries (both zoned and unzoned), the large majority of the points result in sulfur concentrations of 20–40 ppm for the melt in equilibrium with apatite (Fig. 10a). Alternatively, Peng et al. (1997) proposed an experimental calibration of S partitioning between apatite and melt that is controlled by temperature only. At AST (i.e., ~ 900 °C), the apatite/melt partition coefficient for S is 6 and increases at lower temperatures. Using a fixed value of 6, the computed S melt concentrations are mainly between 100 and 200 ppm for the three porphyries (Fig. 10b) and represent a maximum as lower values would be expected at lower temperatures. In both cases, few scattered points from S-rich apatite domains result in much higher apparent S melt concentrations (Fig. 10) and are discussed independently below. One should note that at upper crustal pressure and at fO_2 ranging from NNO + 1 to NNO + 2, sulfate (S^{6+}) would not be the only S species and that some amount of reduced sulfur may also be present (Jugo et al. 2010; Botcharnikov et al. 2011;

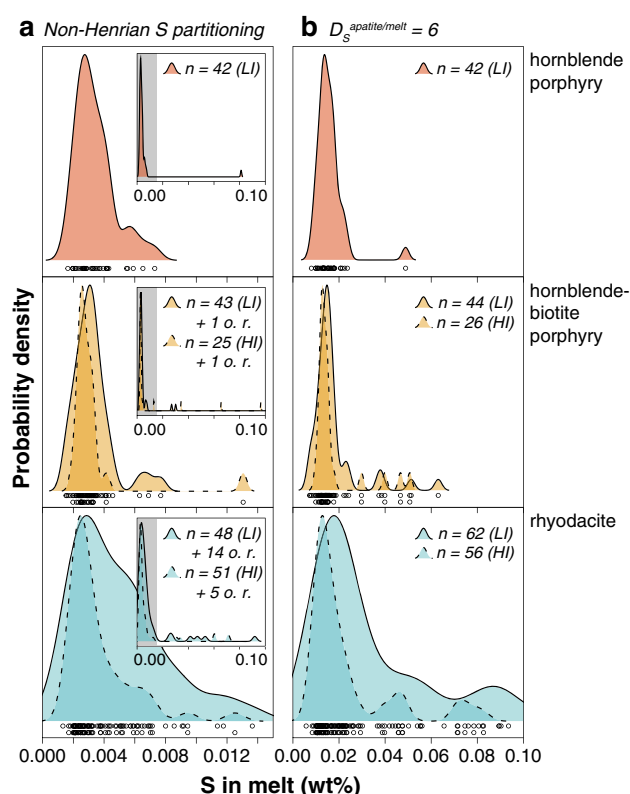


Fig. 10 Probability density of estimated S concentration of the melt based on apatite from the porphyries. **a** Estimate using the non-Henrian partitioning function of Parat et al. (2011b). **b** Estimate using a fixed partition coefficient of 6, which is calculated from the temperature-dependent partition coefficient calibration of Peng et al. (1997) at 900 °C. *o. r.* outside range, *LI* low-intensity EMPA method, *HI* high-intensity EMPA method

Matjuschkin et al. 2016). Therefore, because apatite mainly incorporates sulfate ions (S^{6+}) in its lattice, the melt sulfur concentration we obtain is likely a minimum value and only accounts for the concentration of the sulfate ions in the melt.

S-rich apatite domains

Going from the hornblende porphyry to the rhyodacite, an increasing proportion of points shows higher S values, which even fall outside the calibration range. These are very scattered and seem unlikely to reflect very high melt sulfur concentrations, as the oxidized dacitic melt would be anhydrite saturated at few hundred ppm of S (certainly less than 500 ppm S; Baker and Moretti 2011). Similar S-rich apatites ($SO_3 > 0.5$ wt%) have been reported in a number of natural systems (Streck and Dilles 1998; Parat et al. 2002, 2011a; Streck et al. 2007; Chambefort et al. 2008; Van Hoose et al. 2013), but could not be synthesized experimentally and remain enigmatic. Their common association with anhydrite-saturated magmas suggests that they might have crystallized from abnormally S-enriched melt pockets

(Parat et al. 2011a, b). Van Hoose et al. (2013) also proposed that S-rich apatites from Pinatubo may result from sulfur-fluxing events caused by a degassing underplated body of basalt. However, magmatic anhydrite could not be observed at Corocchohuayco and high S domains of apatite show no trace element similarity or consistency from one grain to another (Fig. 7), suggesting that no uniform process can account for their formation. The only two common characteristics of S-rich apatite domains from Corocchohuayco are their presence in grains showing dissolution/overgrowth textures and their bluer CL response (Fig. 7).

As already mentioned, the dissolution of apatite would be readily facilitated in peraluminous melts (Pichavant et al. 1992). Furthermore, given the hydrous character of the magma at Corocchohuayco, it is likely that sulfur and water fluxing accompanied melting of preexisting lithologies. Therefore, we suggest that the dissolution/overgrowth texture, the variable trace element systematics among different grains and the zoning of apatite grains with S-rich domains (Fig. 7b, c) might be consequences of the partial melting of various apatite-bearing crustal lithologies (proto-plutons, sediments; with apatite of various chemistries) and subsequent crystallization under a high S flux. In this view, apatite cores with chemistry unlike any other apatite in the same rock (e.g., in Fig. 7b, c; possibly including some S-rich cores with various trace element abundances) may be xenocrystic in origin. Partial melting of crustal lithologies promoted apatite dissolution, and sulfur from the volumetrically dominant water-rich dacitic magma would have readily fluxed into the peraluminous melt pocket and promoted the crystallization of S-rich apatite rims upon cooling. This model is consistent with the finding that the porphyries (from the emplacement of the hornblende porphyry to the emplacement of the rhyodacite) record increasing sediment assimilation, proto-pluton cannibalism and even remelting for the rhyodacite (Chelle-Michou et al. 2014, 2015a).

Chlorine concentration of the melt

Estimates from apatite

As noted by Boyce et al. (2014), simple Nernst apatite/melt partition coefficients for Cl cannot be used to estimate the melt Cl concentration. This is because, in apatite, Cl, F and OH occupy the same crystallographic site and their abundance is controlled by apatite stoichiometry, which implies that they cannot be treated in the same way as trace elements. Here, we make use of the recently calibrated thermodynamic apatite/melt chlorine partitioning model of Li and Hermann (2017) using experimental data from Webster et al. (2009) at 200 MPa and 900 °C. We argue that the experimental calibrant conditions are reasonably close to those inferred at the time of apatite crystallization at Corocchohuayco and that the thermodynamic parameters can be

applied to determine the Cl melt content in equilibrium with apatite. According to Li and Hermann (2017):

$$\text{Cl}_{\text{melt}}(\text{wt}\%) = \frac{X_{\text{Cl}}^{\text{ap}}}{X_{\text{OH}}^{\text{ap}}} \frac{1}{K_{\text{Cl-OH}}^{\text{ap-melt}}} \times 10.79, \quad (6)$$

where $X_{\text{Cl}}^{\text{ap}}$ and $X_{\text{OH}}^{\text{ap}}$ are the mole fractions of chlorapatite and hydroxylapatite, respectively, and

$$K_{\text{Cl-OH}}^{\text{ap-melt}} = e^{(25.81 + (X_{\text{Cl}}^{\text{ap}} - X_{\text{OH}}^{\text{ap}}) \times 17.33) \times \frac{10^3}{8.314 \times T}}, \quad (7)$$

with the temperature (T) in K. We have computed the Cl melt concentration at temperatures of 850–800 °C, and 900–850 °C for apatite from the gabbrodiorite complex and from the porphyries, respectively. These temperatures correspond to the most likely crystallization temperature of apatite within these rocks.

Using this method, we obtain Cl melt concentrations of ca. 0.60 ± 0.10 wt% for the gabbrodiorite complex, and ranging from 0.3 to 0.1 wt% for the porphyries (Fig. 11a). Results for the rhyodacite are the most scattered and do not define a clear normally distributed population as for the other samples. The effect of the chosen temperature on the calculated concentration is minimal for apatites from the porphyries, but can affect the results by up to 0.1 wt% for those from the gabbrodiorite complex (Fig. 11a). It is noteworthy that despite having very different Cl concentrations (average of Cl content of 3.4 ± 0.1 wt% in sample 10CC61, 2.2 ± 0.3 wt% in sample 10CC55 and 1.9 ± 0.3 wt% in sample 10CC09), apatites from the three samples of the gabbrodiorite complex record very similar melt

Cl concentrations. Our results further suggest that these large variations of apatite Cl content in the gabbrodiorite can result from variable apatite crystallization temperatures consistent with bulk sample SiO_2 content (lower in sample 10CC61 than in sample 10CC09; Figs. 3, 11a) and/or from small variations in the Cl concentration of the interstitial melt at the time of apatite crystallization (higher in sample 10CC61 than in sample 10CC09).

Estimates from amphibole

Various studies have attempted to retrieve the magma Cl content from amphibole composition (e.g., Sato et al. 2005; Zhang et al. 2012; Giesting and Filiberto 2014). These methods rely on the calibration of the partitioning model for OH/Cl between amphibole and melt. Here, we use the most recent formulation of Giesting and Filiberto (2014) that was calibrated on 39 amphibole analyses of various composition and crystallized under various conditions:

$$K_{\text{Cl}} = \frac{(X_{\text{Cl}}/X_{\text{OH}})_{\text{amphibole}}}{([\text{Cl}]/[\text{OH}])_{\text{melt}}}, \quad (8)$$

$$\ln K_{\text{Cl}} = \frac{6.59K}{\text{Na} + [\text{Al}]_{\square}} - 0.679\text{Mg} + 0.487^{[\text{VI}]\text{Fe}}, \quad (9)$$

where X is the mole fraction of an anion in the W site of amphibole, [Cl] and [OH] are the mole fractions of the designated anions in the melt on a one-oxygen basis, and K, Na, $[\text{Al}]_{\square}$, Mg,

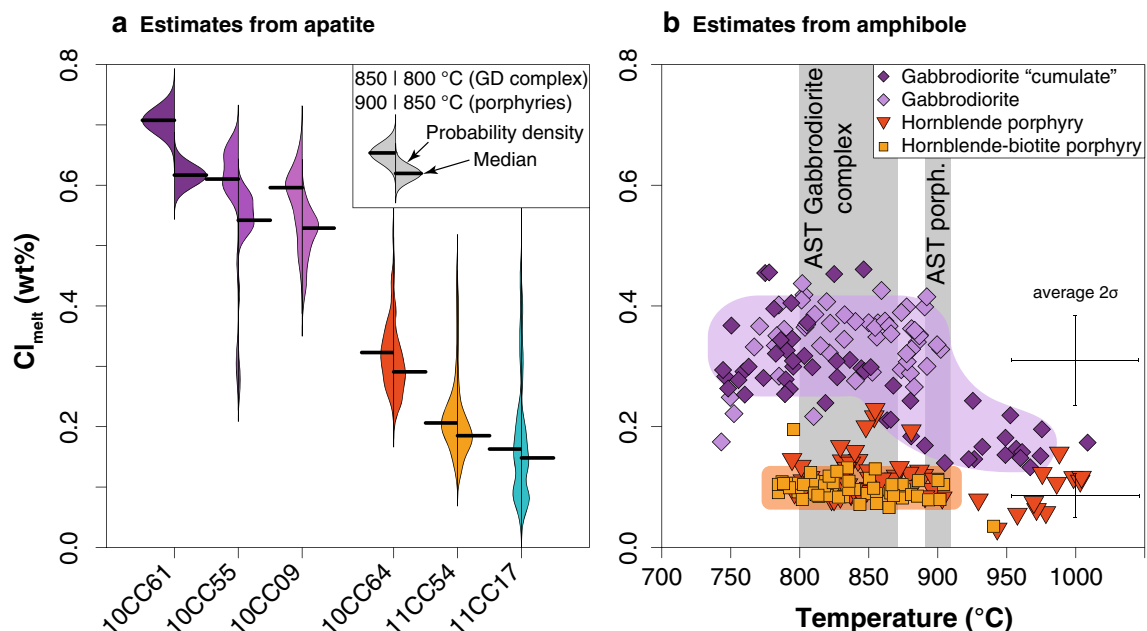
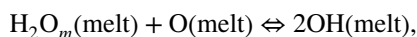


Fig. 11 Melt Cl concentrations estimates based on **a** apatite and **b** amphibole. AST apatite saturation temperature

and ^{VI}Fe are the amounts of each component in the amphibole in apfu. Using Eqs. 8 and 9, we obtain $([\text{Cl}]/[\text{OH}])_{\text{melt}}$ in equilibrium with amphibole at the time of its crystallization.

$[\text{OH}]_{\text{melt}}$ can be determined independently using available knowledge on the speciation of water in silicate melts. The speciation of water is controlled by the dissociation reaction (Stolper 1982; Zhang 1999; Zhang and Ni 2010):



where H_2O_m refers to the molecular H_2O dissolved in the melt. The equilibrium constant of this reaction is

$$K_2 = \frac{[\text{OH}]^2}{[\text{H}_2\text{O}_m][\text{O}]}, \quad (10)$$

where $[\text{H}_2\text{O}_m]$, $[\text{OH}]$ and $[\text{O}]$ are the molar fractions of molecular H_2O , hydroxyl group (not bounded with H) and bridging O atom dissolved in the melt, respectively. For the gabbrodiorite (of basaltic compositions), we use the K_2 temperature-dependent basalt calibration of Lesne et al. (2011) whereas for the porphyries (of dacitic to rhyodacitic compositions) we use the K_2 temperature-dependent dacite calibration of Liu et al. (2004) recommended by Zhang and Ni (2010). In both cases, we have used the amphibole crystallization temperatures obtained by Chelle-Michou et al. (2015a) to calculate the K_2 relevant to each amphibole analyses. In addition, the relation of the different species of water can be expressed as follows (Stolper 1982; Zhang 1999; Zhang and Ni 2010):

$$[\text{H}_2\text{O}_t] = \frac{C/18.015}{C/18.015 + (1 - C)/W}, \quad (11)$$

$$[\text{H}_2\text{O}_t] = [\text{H}_2\text{O}_m] + [\text{OH}]/2, \quad (12)$$

$$[\text{O}] + [\text{H}_2\text{O}_m] + [\text{OH}] = 1, \quad (13)$$

where C is the mass fraction of water in the melt, W is the molar mass of the dry silicate melt and $[\text{H}_2\text{O}_t]$ is the molar fraction of total H_2O in the melt. For each amphibole analysis, C was assumed to be equivalent to the one calculated from amphibole chemistry (Chelle-Michou et al. 2015a) and is always close to the theoretical value at water saturation. For the porphyries, we use an average value of W (33.6 g/mol) calculated from the whole-rock composition. For the gabbrodiorite complex, we estimated the composition of the melt at the time of amphibole saturation (see above) and obtained an average W of 36.1 g/mol. Combining Eqs. 10, 12 and 13, we can derive $[\text{OH}]$ as a function of K_2 and $[\text{H}_2\text{O}_t]$ (see Zhang et al. 2012):

Subsequently, $[\text{OH}]$ can be substituted in Eq. 8 to determine the molar and mass fractions of Cl in the melt in equilibrium with amphibole.

Melt Cl concentrations obtained from amphibole are plotted against the estimated temperature in Fig. 11b. For the gabbrodiorite complex, melt Cl concentration at ca. 975 °C is 0.17 ± 0.03 wt% and gradually increases to 0.37 ± 0.11 wt% at ca. 875 °C. Upon further cooling, the melt Cl concentration remains constant. In contrast, melt Cl concentration for the porphyries remains remarkably constant at 0.10 ± 0.03 wt% from 900 to 775 °C. Cl concentrations obtained from the high-Al amphiboles decrease from 0.16 wt% at 1000 °C to 0.03 wt% at 950 °C. However, the absence of edenite exchange in these high-Al amphiboles suggests that this temperature trend might be an artifact. Nevertheless, the calculated Cl melt concentration is fairly insensitive to temperature and similar values are obtained for the high-Al amphiboles if a fixed temperature of 900 °C is used.

Effect of halogen diffusion and hydrothermal alteration on the Cl and S record

Post-mineral crystallization diffusion and hydrothermal alteration need to be considered if we are to use minerals to estimate the evolution of melt properties during the evolution of the magmatic system. Indeed, both processes would obscure or even overwrite the original record. Hydrothermal experiments conducted on apatite and amphibole have shown that chlorine is a fast-diffusive element in both minerals, with diffusion coefficients that are orders of magnitude higher than for the main crystal-forming cations [4.2×10^{-16} and 2.8×10^{-15} m²/s at 800 °C and 1 GPa for Cl in apatite and amphibole, respectively; Brenan (1994), Su et al. (2015)]. This suggests that at magmatic temperature, any initial Cl zoning acquired during crystal growth should fade away and homogenize within weekly to yearly timescales (Boyce and Hervig 2008; Sato et al. 2017).

The lack of crystal-scale chlorine zoning in apatite and the limited chlorine variability in amphibole from Corocohuayco are consistent with their plutonic (gabbrodiorite complex) to subvolcanic (porphyries) origin, whereby they have been subjected to a long annealing process during magmatic and sub-solidus cooling. If Cl has not been significantly exchanged with a surrounding phase (fluid, melt or Cl-bearing mineral) after the mineral crystallized, the Cl concentration measured on each point of a given crystal should represent an average of the Cl concentration in the entire crystal.

$$[\text{OH}] = 2[\text{H}_2\text{O}_t] + \frac{8[\text{H}_2\text{O}_t] + K_2 - 2[\text{H}_2\text{O}_t]K_2 - \sqrt{K_2} \sqrt{16[\text{H}_2\text{O}_t] - 16[\text{H}_2\text{O}_t]^2 + K_2 - 4[\text{H}_2\text{O}_t]K_2 + 4[\text{H}_2\text{O}_t]^2 K_2}}{K_2 - 4}. \quad (14)$$

In the gabbrodiorite “cumulate”, the preservation of both high-T (> 900 °C) amphibole crystals that record an average low Cl melt concentration (ca. 0.17 wt%) and lower-T (< 900 °C) amphibole crystals that record an average Cl concentration of ca. 0.37 wt% in the same samples (Fig. 11b) suggests that (1) post-crystallization Cl exchange with a surrounding liquid or solid phase was limited. Yet, some amphibole crystals record intra-crystal scatter (of Cl and temperature) that cannot be explained by thermometer calibration or analytical uncertainties (Fig. 9). The observation that results from these grains fall within the array defined by the more chemically homogenous amphibole crystals (Fig. 11), suggesting that diffusion could not entirely erase the original record. This is at odds with the large diffusion coefficients for Cl that would rather suggest that Cl in amphibole would homogenize quicker than in apatite. It highlights the need for a better understanding of halogen diffusion in amphibole.

Despite that only fresh-looking amphiboles and apatites were selected for the present study (within relatively unaltered samples), the effect of potentially unrecognized subsolidus hydrothermal alteration during the porphyry–skarn mineralization may be evaluated. The available fluid inclusion record at Corocochuayco documents the presence of high-salinity brines during the mineralization (30–61 wt% NaCl_{eq}, average of ca. 45 wt% NaCl_{eq}) with homogenization temperatures ranging from > 650 to 170 °C (Maher 2010). If these fluids would have interacted with the already crystallized apatite and amphibole hosted within the porphyries and the gabbrodiorite complex, these minerals would have readily been dramatically enriched in Cl along mineral boundaries, cleavages or fractures [see for example the hydrothermal experiments of Brenan (1994) and Su et al. (2015)].

To our knowledge, no data on the diffusion of sulfur in apatite are available so far. However, due to the incorporation of sulfur in apatite through a coupled substitution (see above), sulfur is expected to diffuse several orders of magnitude slower than Cl in apatite. Therefore, by comparison with Cl and due to the presence of S zoning in some apatite crystals (see Figs. 6, 7), we conclude that post-crystallization diffusion and hydrothermal alteration did not affect the apatite record in our samples.

Chlorine insights into the petrologic evolution of magmas

Estimates of melt chlorine concentration using apatite and amphibole show a wide range of values of 0.1–0.7 wt%, as well as distinct behaviors depending on the mineral used for the calculation (Fig. 11). It is worth noting that these numbers are within the range of Cl melt concentrations of arc magmas (0.01–0.85; Aiuppa et al. 2009). Overall, estimates based on amphibole fall in the lower range or significantly below those based on apatite. While values of

0.2–0.6 wt% (estimated from both apatite and amphibole) seem reasonable for the gabbrodiorite complex (compared to arc basalts and andesite with values up to 0.85 wt%; Aiuppa et al. 2009), values of 0.1 wt% for the porphyries obtained from amphibole are on the low range of typical values for dacite (0.01–0.3 wt%). Indeed, on using Cl fluid/melt partition coefficients between 4.5 and 20 (corresponding to pressures of 100 and 200 MPa, respectively; Zhang et al. 2012), they correspond to a fluid salinity of $\sim 2.0 \pm 1.3$ wt% NaCl_{eq} (i.e., assuming all Cl[−] complexed with Na⁺: with $\text{NaCl}_{\text{eq}} = \text{Cl}_{\text{melt}} \times D_{\text{Cl}}^{\text{fluid/melt}} \times m_{\text{NaCl}}/m_{\text{Cl}}$, where m refers to the molar masses) that is unusually low for pristine high-temperature single-phase magmatic fluids of porphyry copper deposits (typically, 3–10 wt% NaCl_{eq}; Kouzmanov and Pokrovski 2012). In turn, Cl melt concentrations estimated from apatite (0.1–0.3 wt%) result in fluid salinities (1–10 wt% NaCl_{eq}) that are more compatible with the salinity of fluids of porphyry systems.

The plausible causes of this discrepancy between the apatite- and amphibole-based Cl melt concentration estimates might involve (1) systematic measurement errors for F in amphibole, (2) inaccurate calibration of one of the equilibrium constants of the reactions involved (crystal–melt exchange reaction, dissociation of water in the melt) and/or (3) inaccuracy of the estimated temperature and H₂O melt concentration. We conducted sensitivity tests by varying the H₂O melt concentration of ± 1 wt%, the temperature of amphibole crystallization of ± 50 °C and by considering that the amphibole contains 0.1 wt% of F (instead of 0). The results were always within 15% of those we report in Fig. 10, suggesting that the discrepancy would rather come from the calibration of some of the equilibrium constants. Melt Cl concentrations estimated from apatite are probably reasonable estimates for both rock units, but additional constraints are necessary to confirm these results and to understand the cause of the discrepancy between apatite and amphibole estimates. Regardless of the absolute Cl melt concentrations, relative changes from one rock type to another may shed some light on the petrologic processes at stake during magma cooling, crystallization and fluid exsolution.

In the gabbrodiorite complex, few early high-T (> 900 °C) amphiboles record an increase of Cl melt concentration from 0.17 to 0.37 wt% with cooling (Fig. 11b). This likely results from the progressive crystallization of the fluid-undersaturated magma which caused the concurrent enrichment of H₂O, Cl and other incompatible elements (e.g., Zr, P) in the residual melt. This conclusion confirms earlier thoughts that the basaltic magma initially was fluid under-saturated (with ~ 3 wt% H₂O in the melt) and became water saturated (with ~ 5 wt% H₂O) at the time at which most of the amphibole started to crystallize (see discussion in Chelle-Michou et al. 2015a). As the magma kept on cooling, amphibole records a relatively stable Cl melt concentration of

0.37 ± 0.11 wt% down to 750 °C (Fig. 11b). In three samples from the gabbrodiorite complex, apatite records subequal Cl melt concentration of ca. 0.60 wt% (at temperatures of 850–800 °C), small variations of which (± 0.10 wt%) can fully be explained by varying temperatures of apatite crystallization (Fig. 11a). Following the previous line of reasoning, whereby the initial basaltic magma was fluid undersaturated, the initial melt had 0.3–0.4 wt% Cl.

In the porphyries, apatite records an apparent decrease of Cl melt concentration with the relative timing of emplacement of the rocks (Fig. 11a). The largest difference is between the hornblende and the hornblende–biotite porphyries where the Cl concentration estimated from apatite (850–900 °C) drops by 30% (from 0.3 to 0.2 wt%). The hornblende porphyry and the slightly more evolved hornblende–biotite porphyry were suggested to have been sourced from an isotopically homogeneous deep crustal hot zone where they acquired their slightly distinct chemistry through crystal fractionation (Chelle-Michou et al. 2015a). In the deep crust, where the magma is likely fluid undersaturated, crystal fractionation should cause an increase in melt Cl concentration rather than the observed decrease.

Upon further cooling, amphibole records a very stable Cl melt concentration of ~ 0.10 wt%, two to three times smaller than that determined from apatite (Fig. 11). We modeled the melt Cl evolution of a fluid-saturated felsic magma during cooling and outgassing at 100–200 MPa using the fluid/melt partition coefficient of Zhang et al. (2012) and bulk crystal/melt partition coefficients between 0 and 0.5 (Fig. 12). During magmatic cooling, the competing effect of magma crystallization (increase of Cl melt concentration) and fluid exsolution (decrease of Cl melt concentration), and the pressure dependence of Cl fluid/melt partition coefficient, may cause Cl melt concentration to decrease or increase. Accordingly, at 100 MPa melt, Cl enrichment is expected upon cooling, while Cl depletion is expected at 200 MPa (Fig. 12;

see also Cline and Bodnar 1991). It results in average Cl melt concentrations for a fluid-saturated magma emplaced at 100–200 MPa, such as those investigated here, remaining approximately constant during crystallization. This is consistently recorded in the amphibole from the porphyry and possibly provides an external pressure constraint on the emplacement depth of the source pluton at Corocohuayco.

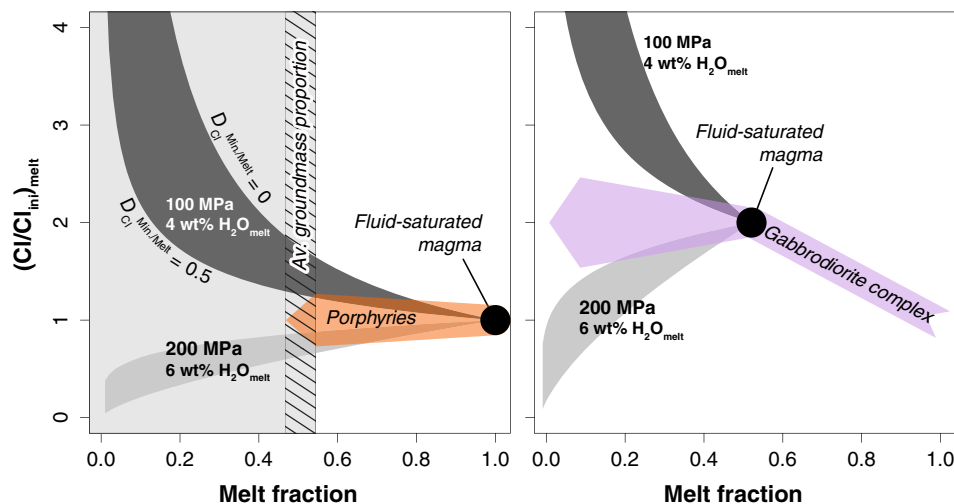
In addition to the effect of pressure, the solubility of Cl in the silicate melt tends to decrease with evolving melt composition (e.g., Webster 2004). Therefore, in the course of magma cooling and evolution of the interstitial melt, the Cl melt concentration would readily decrease upon Cl saturation. Such behavior is not recorded in our data, suggesting that interstitial melt evolution had little influence on the behavior of Cl in the melt, at least down to temperatures of ca. 750 °C for the gabbrodiorite and ca. 800 °C for the porphyries (Fig. 11).

Mass balance constraints on the genesis of the Corocohuayco deposit

The S and Cl melt concentrations determined above can be used to derive mass balance constraints on the minimum volume of magma required to have sourced magmatic–hydrothermal fluids, Cl, S and Cu to the Corocohuayco porphyry–skarn deposit. In addition to the concentration of these elements in the source magma, this exercise requires some estimates of the total inventory of S, Cl and Cu present in or required to form the deposit.

Given the ca. 3 Mt of contained Cu of the Corocohuayco deposit (Chelle-Michou et al. 2015b) and assuming that all this copper is contained in chalcopyrite (which is a reasonable assumption based on drill core logging information), the deposit hosts a minimum of 3 Mt of sulfur in association with copper. Based on mine staff core logging, a chalcopyrite:pyrite proportion of 3:2 can be

Fig. 12 Model for the evolution of the relative Cl concentration of the melt for **a** the porphyries and **b** the gabbrodiorite complex. Gray fields represent the predicted Cl melt concentration computed at 100 and 200 MPa using the pressure-dependent fluid/melt partition coefficient of Zhang et al. (2012) and bulk mineral/melt Cl partition coefficients between 0 and 0.5. Cl_{ini} is the initial melt Cl concentration (at melt fraction of 1)



estimated which adds another 2 Mt of sulfur to the total amount. Assuming that the 5 Mt of reduced S (in the form of H_2S) required for the precipitation of sulfide minerals (i.e., pyrite and chalcopyrite) were formed by disproportionation of SO_2 gas (according to the reaction: $4\text{SO}_2 + 4\text{H}_2\text{O} = \text{H}_2\text{S} + 3\text{HSO}_4^- + 3\text{H}^+$; e.g., Kouzmanov and Pokrovski 2012) a minimum of 20 Mt of S should have been degassed by the cooling sub-porphyry pluton.

A similar calculation can be made for chlorine. Chlorine is the main ligand for Na, K, Fe, Cu, Pb and Zn in hydrothermal fluids, and the required amount of chlorine should account for the transport of these elements. At Corocochuayco, the skarn body is of the order of 100 Mt (Chelle-Michou et al. 2015b). According to drill core logging information, the skarn is largely dominated by garnet, pyroxene and magnetite (> 80%; the rest being clay minerals, carbonates, amphibole and epidote) in garnet:pyroxene:magnetite proportions of 2:1:1. Maher (2010) determined that skarn garnet is dominated by andradite, while pyroxene is a mixture of diopside and hedenbergite. For the sake of simplification, we will assume that only hedenbergite was present. Using these constraints, 35 Mt of metallic iron (Fe) is present within the skarn, with an additional 5 Mt of Fe in sulfides (see above), totaling up to 40 Mt of Fe in the deposit (Fig. 13). Assuming that this iron was exclusively sourced by the magmatic–hydrothermal fluid (i.e., no Fe in the limestone protolith of the skarn), 51 Mt of Cl was necessary to transport iron as FeCl_2 complex. Another 3 Mt of Cl is required to transport the known copper mass of the deposit as CuCl_2^- complex. The total mass of Na, K, Pb, and Zn transported in the ore-forming fluid has not been estimated at Corocochuayco. However, we can estimate their probable amount by comparison with other porphyry systems. Median values for single-phase fluid inclusions at porphyry systems (Kouzmanov and Pokrovski 2012) show that K and Na are typically 2 and 3.7 times more enriched than Fe, while the concentrations of Zn and Pb only correspond to 16 and 5% that of Fe, respectively. Using these values, and considering that these cations are transported as KCl , NaCl , ZnCl_3^- and PbCl_3^- , another 312 Mt of Cl is required. Under the assumptions we have made, a total of 366 Mt of chlorine are required to form the Corocochuayco deposit (Fig. 13).

To compute the mass transfer of volatile and fluid-mobile elements (i.e., S, Cl and Cu) from the cooling pluton to the overlying porphyry–skarn deposit, we used the magma outgassing model of Chelle-Michou et al. (2017) for a fluid-saturated magma with 5 wt% of water. This model considers stepwise degassing of the magma at successive fluid percolation thresholds over the course of magma cooling and crystallization. To quantify uncertainties of the outputs, this model uses a Monte Carlo approach allowing to compute 100,000 solutions by varying simultaneously and randomly all the input parameters (such as starting composition and

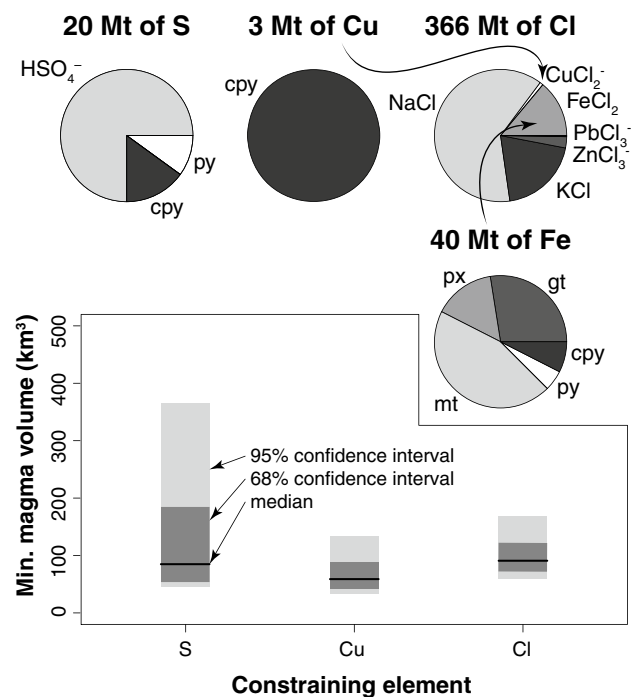


Fig. 13 Estimates of the minimum magma volumes based on S, Cu and Cl mass balance constrained from the Corocochuayco deposit, Peru. The pie charts show the speciation (mineral or complex) of the elements that are constrained by drill core observations (S, Cu, Fe) and by assuming similar intercationic ratio (e.g., Na/Fe, K/Fe) as fluid-inclusion data from porphyry systems worldwide (for Cl). Arrows indicate that the masses of Cl complexes with Cu and Fe derived from the estimated masses of Cu and Fe in the mineral deposit. *Cpy* chalcopyrite, *gt* andradite garnet, *mt* magnetite, *px* hedenbergite pyroxene, *py* pyrite

partition coefficient) within their reasonable range of values. Starting S and Cl concentrations were those estimated from apatite and were varied from 20 to 200 ppm for S (depending on the partition coefficient used; Fig. 10) and from 0.2 to 0.3 wt% for Cl (Fig. 11), respectively. Initial melt Cu concentrations were assumed to be 20–50 ppm as commonly advocated for such intermediate arc magmas (Cline and Bodnar 1991; Steinberger et al. 2013; Chiaradia 2014). Fluid/melt partition coefficients for S were computed from the calibration of Masotta et al. (2016) using the whole-rock composition of the porphyries and ranged from 2 to 15. To account for the evolution of the interstitial melt during cooling, we extend this range to 50. Fluid/melt partition coefficients for Cl were 4.5–20 (calculated from Zhang et al. 2012 at 100 and 200 MPa), while those for Cu were computed from the salinity of the degassed fluid according to Tattitch and Blundy (2017).

Within the range of input parameters, we determine that a minimum of 43–365 km³ (median of 81 km³), 33–131 km³ (median of 60 km³) and 60–169 km³ (median of 91 km³) of magma is required to source the 20 Mt of S, 3 Mt of Cu and

366 Mt of Cl to the Corocochuayco deposit, respectively (Fig. 13). Magma volumes calculated using S, Cu and Cl mass balance constraints from the ore deposit at Corocochuayco compare very well to each other and suggest that a volume of magma in the order of 100 km³ most likely sourced the deposit (Fig. 13). It is also noteworthy that these volumes are in the range of those estimated from field exposure for the Luhr Hill Granite (~ 65 km³) that sourced porphyry copper deposits from the tilted Yerington District which has a very similar Cu endowment of ~ 4.1 Mt of Cu (Cline and Bodnar 1991; Dilles and Proffett 1995).

In contrast to the figures above, high-precision zircon U–Pb dates and thermal modeling returned a volume of 500–2000 km³ for the pluton below Corocochuayco (Caricchi et al. 2014). Another volume estimate can be made considering that the ore-related magmatic system assembled over a maximum of 100 ka (Chelle-Michou et al. 2015b). Assuming typical magma fluxes of 0.001 to 0.01 km³/a in magmatic arc setting (de Saint Blanquat et al. 2011), a maximum magma volume of 100 to 1000 km³ can be estimated (see also Chelle-Michou et al. 2017). The differences between mass balance and geochronology-based volume estimates may indicate that (1) only a small fraction of the total budget of Cu, Fe and S could have been extracted and precipitated, and/or (2) other deposits in the immediate vicinity of Corocochuayco (e.g., Tintaya, Ccatun Pucara, Quechua and Antapaccay with a total of 13 Mt of Cu; Chelle-Michou et al. 2015b) may have been sourced by the same body of magma at depth (corresponding to a minimum of 143–570 km³ using the same constraints as above).

Conclusions

Available partitioning models based on apatite and amphibole have been used to retrieve the S and Cl melt concentrations of magmas from the Corocochuayco magmatic suite. We show that the estimated absolute concentrations may vary up to a factor of 3, depending on the partitioning model or the mineral that is used. This highlights the strong need for a better understanding of the partitioning of S and Cl between magma, minerals and fluids for a range of compositions and *P–T* conditions. Despite the large uncertainties associated with our results, we show that S and Cl data from apatite and amphibole can provide useful information on the volatile budget and evolution of magmas.

The sulfur record in apatite from Corocochuayco is consistent with the evolution of the magmatic system from being dominated by S^{2–} (reduced) at ~ 40 Ma to being dominated by S⁶⁺ (oxidized) at the time of porphyry emplacement and ore formation. Estimated initial melt S concentrations of 20–200 ppm for the porphyry magmas imply that a minimum of 43 to 365 km³ (median of 81 km³) of magma is required to

source the Corocochuayco deposit with its known amount of S (~ 5 Mt). This volume estimate is compatible with the volume required to explain the Cu endowment of the deposit (3 Mt; 33–131 km³, median of 60 km³). These data suggest that no specific S enrichment is required to form this economic porphyry copper deposit. This view contrasts with findings from other systems where critical amounts of S are thought to have been sourced by co-magmatic basalts (Keith et al. 1997; Hattori and Keith 2001; Maughan et al. 2002; Halter et al. 2002, 2005; Nadeau et al. 2010, 2016; Steinberger et al. 2013; Blundy et al. 2015). Nevertheless, this concurs with the lack of evidence for mafic magma associated with the porphyries at Corocochuayco (Chelle-Michou et al. 2015a). Furthermore, the similarity of the minimum magma volume estimate based on Cl (60–169 km³) with those based on Cu (33–131 km³) and S (43–365 km³), suggests that the amount of Cl in the magma is at least as critical as the amount of S and Cu to form a porphyry deposit. In other words, magma with high Cu (> 100 ppm) and S (> 500 ppm) content, but normal Cl content (ca. 3000 ppm) would not necessarily have an enhanced metallogenic potential compared to those that formed the Corocochuayco deposit.

More than the amount of S in the magma, the shift from reduced (NNO ± 1) to oxidized magma (NNO + 1 to NNO + 2) probably was a critical factor for the genesis of the Corocochuayco deposit. While sulfide saturation in the lower crust inevitably drives the amount of Cu down during magmatic evolution of calc-alkaline magmatic suites (Chiaradia 2014), the oxidation state of sulfur can dramatically change upon magma ascent and decompression (Matjuschkin et al. 2016). Indeed, for a magma having *f*O₂ buffered around NNO + 1 to NNO + 2 such as the ore-forming porphyries at Corocochuayco, magmatic sulfur is dominantly a reduced species at lower crustal pressures (Matjuschkin et al. 2016), but is dominantly in the form of more oxidized sulfates at upper crustal pressures. This contrasts with magmas buffered at around NNO such as those of the gabbrodiorite complex where sulfur is dominantly in reduced form throughout the thickness of the crust. We suggest that the oxidized character of sulfur at upper crustal pressure (100–200 MPa), where the sub-porphyry plutons typically assemble and degas (Sillitoe 2010), facilitates exsolution of S and Cu into the magmatic fluid rather than their sequestration into magmatic sulfides.

Using available partitioning models for apatite and amphibole, we were unable to determine consistent melt Cl concentrations from both minerals. While estimates based on apatite seem to provide more reasonable absolute values in the order of 1000 s of ppm, estimates based on amphibole are lower but present more convincing relative variations of Cl melt concentration as a function of temperature. Cl data confirm that the basaltic magma at the origin of the gabbrodiorite complex was initially fluid undersaturated and

that the melt Cl content increased with magma cooling until ca. 900 °C. At this point, the Cl content remained constant, consistent with modeling of magma cooling and fluid exsolution. For the porphyries, the Cl melt concentration remains constant all along the entire cooling path. This confirms that the felsic magma was initially fluid saturated, and that magma emplacement cooling, crystallization and degassing took place at 100–200 MPa (Chelle-Michou et al. 2015a).

Acknowledgements Anders McCarthy and Björn Baresel are thanked for their skilled technical support during electron microprobe analyses, and Jean-Marie Boccard is greatly acknowledged for thin section preparation. This study was funded by the Swiss National Science Foundation (projects No 200020-126896 and 200020-137663). Logistical support by Xstrata Tintaya SA during fieldwork is greatly appreciated. Early discussions with John Dilles and Bruno Scaillet helped to improve the quality of this paper. We thank the editor and the two anonymous reviewers for insightful comments and suggestions that considerably improved the content of this contribution.

Open Access This article is distributed under the terms of the Creative Commons Attribution 4.0 International License (<http://creativecommons.org/licenses/by/4.0/>), which permits unrestricted use, distribution, and reproduction in any medium, provided you give appropriate credit to the original author(s) and the source, provide a link to the Creative Commons license, and indicate if changes were made.

References

- Aiuppa A, Baker DR, Webster JD (2009) Halogens in volcanic systems. *Chem Geol* 263:1–18. <https://doi.org/10.1016/j.chemgeo.2008.10.005>
- Anderson JL, Smith DR (1995) The effects of temperature and fO_2 on the Al-in-hornblende barometer. *Am Min* 80:549–559
- Baker DR, Moretti R (2011) Modeling the solubility of sulfur in magmas: a 50-year old geochemical challenge. *Rev Min Geochem* 73:167–213. <https://doi.org/10.2138/rmg.2011.73.7>
- Baker DR, Alletti M (2012) Fluid saturation and volatile partitioning between melts and hydrous fluids in crustal magmatic systems: the contribution of experimental measurements and solubility models. *Earth Sci Rev* 114(3–4):298–324. <https://doi.org/10.1016/j.earscirev.2012.06.005>
- Bao B, Webster JD, Zhang D-H, Goldoff BA, Zhang R-Z (2016) Compositions of biotite, amphibole, apatite and silicate melt inclusions from the Tongchang mine, Dexing porphyry deposit, SE China: implications for the behavior of halogens in mineralized porphyry systems. *Ore Geol Rev* 79:443–462. <https://doi.org/10.1016/j.oregeorev.2016.05.024>
- Blundy J, Cashman K (2001) Ascent-driven crystallisation of dacite magmas at Mount St Helens, 1980–1986. *Contrib Min Petrol* 140:631–650
- Blundy J, Mavrogenes J, Tattitch B, Sparks S, Gilmer A (2015) Generation of porphyry copper deposits by gas-brine reaction in volcanic arcs. *Nature Geosci* 8:235–240. <https://doi.org/10.1038/ngeo2351>
- Botcharnikov RE, Linnen RL, Wilke M, Holtz F, Jugo PJ, Berndt J (2011) High gold concentrations in sulphide-bearing magma under oxidizing conditions. *Nature Geosci* 4:112–115. <https://doi.org/10.1038/ngeo1042>
- Boyce JW, Hervig RL (2008) Magmatic degassing histories from apatite volatile stratigraphy. *Geology* 36:63–66. <https://doi.org/10.1130/g24184a.1>
- Boyce JW, Tomlinson SM, McCubbin FM, Greenwood JP, Treiman AH (2014) The lunar apatite paradox. *Science* 344:400–402. <https://doi.org/10.1126/science.1250398>
- Brenan J (1994) Kinetics of fluorine, chlorine and hydroxyl exchange in fluorapatite. *Chem Geol* 110:195–210. [https://doi.org/10.1016/0009-2541\(93\)90254-G](https://doi.org/10.1016/0009-2541(93)90254-G)
- Candela PA, Holland HD (1984) The partitioning of copper and molybdenum between silicate melts and aqueous fluids. *Geochim Cosmochim Acta* 48:373–380. [https://doi.org/10.1016/0016-7037\(84\)90257-6](https://doi.org/10.1016/0016-7037(84)90257-6)
- Caricchi L, Simpson G, Schaltegger U (2014) Zircons reveal magma fluxes in the Earth's crust. *Nature* 511:457–461. <https://doi.org/10.1038/nature13532>
- Chambefort I, Dilles JH, Kent AJR (2008) Anhydrite-bearing andesite and dacite as a source for sulfur in magmatic-hydrothermal mineral deposits. *Geology* 36:719. <https://doi.org/10.1130/G24920A.1>
- Chambefort I, Dilles JH, Longo AA (2013) Amphibole geochemistry of the Yanacocha volcanics, Peru: evidence for diverse sources of magmatic volatiles related to gold ores. *J Petrol* 54:1017–1046. <https://doi.org/10.1093/petrology/egt004>
- Chelle-Michou C, Chiaradia M, Ovtcharova M, Ulianov A, Wotzlav J-F (2014) Zircon petrochronology reveals the temporal link between porphyry systems and the magmatic evolution of their hidden plutonic roots (the Eocene Corocochuayco deposit, Peru). *Lithos* 198–199:129–140. <https://doi.org/10.1016/j.lithos.2014.03.017>
- Chelle-Michou C, Chiaradia M, Béguélin P, Ulianov A (2015a) Petrological evolution of the magmatic suite associated with the Corocochuayco Cu(–Au–Fe) Porphyry–skarn deposit, Peru. *J Petrol* 56:1829–1862. <https://doi.org/10.1093/petrology/egv056>
- Chelle-Michou C, Chiaradia M, Selby D, Ovtcharova M, Spinkings RA (2015b) High-resolution geochronology of the Corocochuayco Porphyry–skarn deposit, Peru: a rapid product of the incaic orogeny. *Econ Geol* 110:423–443. <https://doi.org/10.2113/econgeo.110.2.423>
- Chelle-Michou C, Rottier B, Caricchi L, Simpson G (2017) Tempo of magma degassing and the genesis of porphyry copper deposits. *Sci Rep* 7:40566. <https://doi.org/10.1038/srep40566>
- Chiaradia M (2014) Copper enrichment in arc magmas controlled by overriding plate thickness. *Nature Geosci* 7:43–46. <https://doi.org/10.1038/ngeo2028>
- Cline JS, Bodnar RJ (1991) Can economic porphyry copper mineralization be generated by a typical calc-alkaline melt? *J Geophys Res* 96:8113–8126. <https://doi.org/10.1029/91JB00053>
- Costa F, Scaillet B, Pichavant M (2004) Petrological and experimental constraints on the pre-eruption conditions of Holocene Dacite from Volcán San Pedro (36°S, Chilean Andes) and the Importance of Sulphur in Silicic Subduction-related Magmas. *J Petrol* 45:855–881. <https://doi.org/10.1093/petrology/egg114>
- Coulson I, Dipple G, Raudsepp M (2001) Evolution of HF and HCl activity in magmatic volatiles of the gold-mineralized Emerald Lake pluton, Yukon Territory, Canada. *Miner Deposita* 36:594–606. <https://doi.org/10.1007/s001260100191>
- de Saint Blanquat M, Horsman E, Habert G, Morgan S, Vanderhaeghe O, Law R, Tikoff B (2011) Multiscale magmatic cyclicity, duration of pluton construction, and the paradoxical relationship between tectonism and plutonism in continental arcs. *Tectonophysics* 500:20–33. <https://doi.org/10.1016/j.tecto.2009.12.009>
- Dilles JH, Proffett JM (1995) Metallogenesis of the Yerington batholith, Nevada. In: *Porphyry copper deposits of the American Cordillera*. Arizona Geological Society Digest, pp 306–315
- Dreher ST, Macpherson CG, Pearson DG, Davidson JP (2005) Re-Os isotope studies of Mindanao adakites: implications for sources of metals and melts. *Geology* 33:957. <https://doi.org/10.1130/G21755.1>

- Erdmann S, Martel C, Pichavant M, Kushnir A (2014) Amphibole as an archivist of magmatic crystallization conditions: problems, potential, and implications for inferring magma storage prior to the paroxysmal 2010 eruption of Mount Merapi, Indonesia. *Contrib Min Petrol* 167:1016. <https://doi.org/10.1007/s00410-014-1016-4>
- Frank MR, Candela PA, Piccoli PM (2003) Alkali exchange equilibria between a silicate melt and coexisting magmatic volatile phase: an experimental study at 800 °C and 100 MPa. *Geochim Cosmochim Acta* 67:1415–1427. [https://doi.org/10.1016/S0016-7037\(02\)01181-X](https://doi.org/10.1016/S0016-7037(02)01181-X)
- Giesting PA, Filiberto J (2014) Quantitative models linking igneous amphibole composition with magma Cl and OH content. *Am Min* 99:852–865. <https://doi.org/10.2138/am.2014.4623>
- Goldoff B, Webster JD, Harlov DE (2012) Characterization of fluor-chlorapatites by electron probe microanalysis with a focus on time-dependent intensity variation of halogens. *Am Min* 97:1103–1115. <https://doi.org/10.2138/am.2012.3812>
- Halter WE, Pettke T, Heinrich CA (2002) The origin of Cu/Au ratios in porphyry-type ore deposits. *Science* 296:1844–1846. <https://doi.org/10.1126/science.1070139>
- Halter WE, Heinrich CA, Pettke T (2005) Magma evolution and the formation of porphyry Cu-Au ore fluids: evidence from silicate and sulfide melt inclusions. *Min Deposita* 39:845–863. <https://doi.org/10.1007/s00126-004-0457-5>
- Harrison TM, Watson EB (1984) The behavior of apatite during crustal anatexis: equilibrium and kinetic considerations. *Geochim Cosmochim Acta* 48:1467–1477. [https://doi.org/10.1016/0016-7037\(84\)90403-4](https://doi.org/10.1016/0016-7037(84)90403-4)
- Hattori KH, Keith J (2001) Contribution of mafic melt to porphyry copper mineralization: evidence from Mount Pinatubo, Philippines, and Bingham Canyon, Utah, USA. *Min Deposita* 36:799–806. <https://doi.org/10.1007/s001260100209>
- Hedenquist JW, Lowenstern JB (1994) The role of magmas in the formation of hydrothermal ore deposits. *Nature* 370:519–527. <https://doi.org/10.1038/370519a0>
- Holland T, Blundy J (1994) Non-ideal interactions in calcic amphiboles and their bearing on amphibole-plagioclase thermometry. *Contrib Min Petrol* 116:433–447. <https://doi.org/10.1007/BF00310910>
- Jugo PJ, Wilke M, Botcharnikov RE (2010) Sulfur K-edge XANES analysis of natural and synthetic basaltic glasses: implications for S speciation and S content as function of oxygen fugacity. *Geochim Cosmochim Acta* 74:5926–5938. <https://doi.org/10.1016/j.gca.2010.07.022>
- Keith JD, Whitney JA, Hattori K, Ballantyne GH, Christiansen EH, Barr DL, Cannan TM, Hook CJ (1997) The role of magmatic sulfides and mafic alkaline magmas in the Bingham and Tintic mining districts, Utah. *J Petrol* 38:1679–1690. <https://doi.org/10.1093/ptro/38.12.1679>
- Konecke BA, Fiege A, Simon AC, Parat F, Stechern A (2017) Co-variability of S^{6+} , S^{4+} , and S^{2-} in apatite as a function of oxidation state: implications for a new oxybarometer. *Am Min* 102:548–557. <https://doi.org/10.2138/am-2017-5907>
- Kouzmanov K, Pokrovski GS (2012) Hydrothermal controls on metal distribution in porphyry Cu (-Mo-Au) systems. *Soc Econ Geol Spec Publ* 16:573–618
- Leake BE, Woolley AR, Arps CES et al (1997) Nomenclature of amphiboles; report of the subcommittee on amphiboles of the international mineralogical association, commission on new minerals and mineral names. *Can Mineral* 35:219–246
- Lesne P, Scaillet B, Pichavant M, Iacono-Marziano G, Beny J-M et al (2011) The H_2O solubility of alkali basaltic melts: an experimental study. *Contrib Min Petrol* 162:133–151. <https://doi.org/10.1007/s00410-010-0588-x>
- Li H, Hermann J (2017) Chlorine and fluorine partitioning between apatite and sediment melt at 2.5 GPa, 800 °C: a new experimentally derived thermodynamic model. *Am Mineral* 102:580–594. <https://doi.org/10.2138/am-2017-5891>
- Liu Y, Comodi P (1993) Some aspects of the crystal-chemistry of apatites. *Min Mag* 57:709–719. <https://doi.org/10.1180/minmag.1993.057.389.15>
- Liu Y, Behrens H, Zhang Y (2004) The speciation of dissolved H_2O in dacitic melt. *Am Min* 89:277–284. <https://doi.org/10.2138/am-2004-2-304>
- Maher KC (2010) Skarn alteration and mineralization at Corocohuayco, Tintaya District, Peru. *Econ Geol* 105:263–283. <https://doi.org/10.2113/gsecongeo.105.2.263>
- Masotta M, Keppler H, Chaudhari A (2016) Fluid-melt partitioning of sulfur in differentiated arc magmas and the sulfur yield of explosive volcanic eruptions. *Geochim Cosmochim Acta* 176:26–43. <https://doi.org/10.1016/j.gca.2015.12.014>
- Matjuschkin V, Blundy JD, Brooker RA (2016) The effect of pressure on sulphur speciation in mid- to deep-crustal arc magmas and implications for the formation of porphyry copper deposits. *Contrib Min Petrol* 171:1–25. <https://doi.org/10.1007/s00410-016-1274-4>
- Maughan D, Keith J, Christiansen E, Pulsipher T, Hattori KH, Evans N (2002) Contributions from mafic alkaline magmas to the Bingham porphyry Cu-Au-Mo deposit, Utah, USA. *Miner Deposita* 37:14–37. <https://doi.org/10.1007/s00126-001-0228-5>
- Nadeau O, Williams-Jones AE, Stix J (2010) Sulphide magma as a source of metals in arc-related magmatic hydrothermal ore fluids. *Nature Geosci* 3:501–505. <https://doi.org/10.1038/ngeo899>
- Nadeau O, Stix J, Williams-Jones AE (2016) Links between arc volcanoes and porphyry-epithermal ore deposits. *Geology* 44:11–14. <https://doi.org/10.1130/G37262.1>
- Parat F, Dungan MA, Streck MJ (2002) Anhydrite, pyrrhotite, and sulfur-rich apatite: tracing the sulfur evolution of an Oligocene andesite (Eagle Mountain, CO, USA). *Lithos* 64:63–75. [https://doi.org/10.1016/S0024-4937\(02\)00155-X](https://doi.org/10.1016/S0024-4937(02)00155-X)
- Parat F, Holtz F, Klügel A (2011a) S-rich apatite-hosted glass inclusions in xenoliths from La Palma: constraints on the volatile partitioning in evolved alkaline magmas. *Contrib Mineral Petrol* 162:463–478. <https://doi.org/10.1007/s00410-011-0606-7>
- Parat F, Holtz F, Streck MJ (2011b) Sulfur-bearing magmatic accessory minerals. *Rev Min Geochem* 73:285–314. <https://doi.org/10.2138/rmg.2011.73.10>
- Patiño Douce AE (1997) Generation of metaluminous A-type granites by low-pressure melting of calc-alkaline granitoids. *Geology* 25:743–746. [https://doi.org/10.1130/0091-7613\(1997\)025<0743:GOMATG>2.3.CO;2](https://doi.org/10.1130/0091-7613(1997)025<0743:GOMATG>2.3.CO;2)
- Peng G, Luhr JF, McGee JJ (1997) Factors controlling sulfur concentrations in volcanic apatite. *Am Min* 82:1210–1224. <https://doi.org/10.2138/am-1997-11-1217>
- Pettke T, Oberli F, Heinrich CA (2010) The magma and metal source of giant porphyry-type ore deposits, based on lead isotope microanalysis of individual fluid inclusions. *Earth Planet Sci Lett* 296:267–277. <https://doi.org/10.1016/j.epsl.2010.05.007>
- Pichavant M, Montel J-M, Richard LR (1992) Apatite solubility in peraluminous liquids: experimental data and an extension of the Harrison-Watson model. *Geochim Cosmochim Acta* 56:3855–3861. [https://doi.org/10.1016/0016-7037\(92\)90178-L](https://doi.org/10.1016/0016-7037(92)90178-L)
- Pokrovski GS, Kokh MA, Guillaume D et al (2015) Sulfur radical species form gold deposits on Earth. *Proc Natl Acad Sci USA* 112:13484–13489. <https://doi.org/10.1073/pnas.1506378112>
- Rasmussen KL, Mortensen JK (2013) Magmatic petrogenesis and the evolution of (F:Cl:OH) fluid composition in barren and tungsten skarn-associated plutons using apatite and biotite compositions: Case studies from the northern Canadian Cordillera. *Ore Geol Rev* 50:118–142. <https://doi.org/10.1016/j.oregeorev.2012.09.006>
- Ridolfi F, Renzulli A (2012) Calcic amphiboles in calc-alkaline and alkaline magmas: thermobarometric and chemometric empirical

- equations valid up to 1130°C and 2.2 GPa. *Contrib Mineral Petrol* 163:877–895. <https://doi.org/10.1007/s00410-011-0704-6>
- Rouse RC, Dunn PJ (1982) A contribution to the crystal chemistry of ellestadite and the silicate sulfate apatites. *Am Min* 67:90–96
- Sato H, Holtz F, Behrens H, Botcharnikov RE, Nakada S (2005) Experimental Petrology of the 1991–1995 Unzen Dacite, Japan. Part II: Cl/OH partitioning between hornblende and melt and its implications for the origin of oscillatory zoning of hornblende phenocrysts. *J Petrol* 46:339–354. <https://doi.org/10.1093/petrology/egh078>
- Sato H, Holtz F, Botcharnikov RE, Nakada S (2017) Intermittent generation of mafic enclaves in the 1991–1995 dacite of Unzen Volcano recorded in mineral chemistry. *Contrib Min Petrol* 172:22
- Scailliet B, Evans BW (1999) The 15 June 1991 eruption of Mount Pinatubo. I. Phase equilibria and pre-eruption P-T-fO₂-fH₂O conditions of the dacite magma. *J Petrol* 40:381–411. <https://doi.org/10.1093/petroj/40.3.381>
- Scott JAJ, Humphreys MCS, Mather TA, Pyle DM, Stock MJ (2015) Insights into the behaviour of S, F, and Cl at Santiaguito Volcano, Guatemala, from apatite and glass. *Lithos* 232:375–394. <https://doi.org/10.1016/j.lithos.2015.07.004>
- Sillitoe RH (2010) Porphyry copper systems. *Econ Geol* 105:3–41. <https://doi.org/10.2113/gsecongeo.105.1.3>
- Simon AC, Ripley EM (2011) The role of magmatic sulfur in the formation of ore deposits. *Rev Min Geochem* 73:513–578. <https://doi.org/10.2138/rmg.2011.73.16>
- Simon AC, Pettke T, Candela PA, Piccoli PM, Heinrich CA (2004) Magnetite solubility and iron transport in magmatic–hydrothermal environments. *Geochim Cosmochim Acta* 68:4905–4914. <https://doi.org/10.1016/j.gca.2004.05.033>
- Simon AC, Pettke T, Candela PA, Piccoli PM, Heinrich CA (2006) Copper partitioning in a melt vapor brine magnetite pyrrhotite assemblage. *Geochim Cosmochim Acta* 70:5583–5600. <https://doi.org/10.1016/j.gca.2006.08.045>
- Steinberger I, Hinks D, Driesner T, Heinrich CA (2013) Source plutons driving porphyry copper ore formation: combining geomagnetic data, thermal constraints, and chemical mass balance to quantify the magma chamber beneath the Bingham Canyon deposit. *Econ Geol* 108:605–624. <https://doi.org/10.2113/econgeo.108.4.605>
- Stock MJ, Humphreys MCS, Smith VC, Johnson RD, Pyle DM, EIMF (2015) New constraints on electron-beam induced halogen migration in apatite. *Am Min* 100:281–293. <https://doi.org/10.2138/am-2015-4949>
- Stolper E (1982) The speciation of water in silicate melts. *Geochim Cosmochim Acta* 46:2609–2620. [https://doi.org/10.1016/0016-7037\(82\)90381-7](https://doi.org/10.1016/0016-7037(82)90381-7)
- Stormer JC Jr, Pierson ML, Tacker RC (1993) Variation of F and Cl X-ray intensity due to anisotropic diffusion in apatite. *Am Min* 78:641–648
- Streck MJ, Dilles JH (1998) Sulfur evolution of oxidized arc magmas as recorded in apatite from a porphyry copper batholith. *Geology* 26:523–526. [https://doi.org/10.1130/0091-7613\(1998\)026<0523:SEOOAM>2.3.CO;2](https://doi.org/10.1130/0091-7613(1998)026<0523:SEOOAM>2.3.CO;2)
- Streck MJ, Broderick CA, Halter WE (2007) Origin of sulfur rich apatite in silicic, calc-alkaline magmas. *Geochimica et Cosmochimica Acta Supplement* 71:A979
- Su W, Baker DR, Pu L, Bai L, Liu X, O'Shaughnessy C (2015) Chlorine-hydroxyl diffusion in pargasitic amphibole. *Am Min* 100:138–147. <https://doi.org/10.2138/am-2015-4779>
- Tattitch BC, Blundy JD (2017) Cu–Mo partitioning between felsic melts and saline-aqueous fluids as a function of $X_{\text{NaCl}_{\text{eq}}}$, $f\text{O}_2$, and $f\text{S}_2$. *Am Min* 102:1987–2006. <https://doi.org/10.2138/am-2017-5998>
- Teiber H, Scharrer M, Marks MAW, Arzamastsev AA, Wenzel T, Markl G (2015) Equilibrium partitioning and subsequent re-distribution of halogens among apatite–biotite–amphibole assemblages from mantle-derived plutonic rocks: complexities revealed. *Lithos* 220–223:221–237. <https://doi.org/10.1016/j.lithos.2015.02.015>
- Tepper JH, Kuehner SM (1999) Complex zoning in apatite from the Idaho batholith: a record of magma mixing and intracrystalline trace element diffusion. *Am Min* 84:581–595. <https://doi.org/10.2138/am-1999-0412>
- Van Hoose AE, Streck MJ, Pallister JS, Wälle M (2013) Sulfur evolution of the 1991 Pinatubo magmas based on apatite. *J Volcanol Geotherm Res* 257:72–89. <https://doi.org/10.1016/j.jvolgeores.2013.03.007>
- Walker BA, Klemetti EW, Grunder AL, Dilles JH, Tepley FJ, Giles D (2013) Crystal reaming during the assembly, maturation, and waning of an eleven-million-year crustal magma cycle: thermobarometry of the Aucanquilcha Volcanic cluster. *Contrib Mineral Petrol* 165:663–682. <https://doi.org/10.1007/s00410-012-0829-2>
- Wallace PJ (2005) Volatiles in subduction zone magmas: concentrations and fluxes based on melt inclusion and volcanic gas data. *J Volcanol Geotherm Res* 140:217–240. <https://doi.org/10.1016/j.jvolgeores.2004.07.023>
- Wallace PJ, Edmonds M (2011) The sulfur budget in magmas: evidence from melt inclusions, submarine glasses, and volcanic gas emissions. *Rev Min Geochem* 73:215–246. <https://doi.org/10.2138/rmg.2011.73.8>
- Webster JD (2004) The exsolution of magmatic hydrosaline chloride liquids. *Chem Geol* 210:33–48. <https://doi.org/10.1016/j.chemgeo.2004.06.003>
- Webster JD, Botcharnikov RE (2011) Distribution of sulfur between melt and fluid in S–O–H–C–Cl-bearing magmatic systems at shallow crustal pressures and temperatures. *Rev Min Geochem* 73:247–283. <https://doi.org/10.2138/rmg.2011.73.9>
- Webster JD, Tappen CM, Mandeville CW (2009) Partitioning behavior of chlorine and fluorine in the system apatite–melt–fluid. II: felsic silicate systems at 200 MPa. *Geochim Cosmochim Acta* 73:559–581. <https://doi.org/10.1016/j.gca.2008.10.034>
- Williams TJ, Candela PA, Piccoli PM (1995) The partitioning of copper between silicate melts and two-phase aqueous fluids: an experimental investigation at 1 kbar, 800 °C and 0.5 kbar, 850 °C. *Contrib Min Petrol* 121:388–399. <https://doi.org/10.1007/s004100050104>
- Williams TJ, Candela PA, Piccoli PM (1997) Hydrogen-alkali exchange between silicate melts and two-phase aqueous mixtures: an experimental investigation. *Contrib Min Petrol* 128:114–126. <https://doi.org/10.1007/s004100050298>
- Williams-Jones AE, Heinrich CA (2005) 100th anniversary special paper: vapor transport of metals and the formation of magmatic–hydrothermal ore deposits. *Econ Geol* 100:1287–1312. <https://doi.org/10.2113/gsecongeo.100.7.1287>
- Young EJ, Myers AT, Munson EL, Conklin NM (1969) Mineralogy and geochemistry of fluorapatite from Cerro de Mercado, Durango, Mexico. In: US Geological Survey Professional Paper 650-D, pp 84–93
- Zajacz Z, Halter W (2009) Copper transport by high temperature, sulfur-rich magmatic vapor: evidence from silicate melt and vapor inclusions in a basaltic andesite from the Villarrica volcano (Chile). *Earth Planet Sci Lett* 282:115–121. <https://doi.org/10.1016/j.epsl.2009.03.006>
- Zajacz Z, Seo JH, Candela PA et al (2010) Alkali metals control the release of gold from volatile-rich magmas. *Earth Planet Sci Lett* 297:50–56. <https://doi.org/10.1016/j.epsl.2010.06.002>
- Zajacz Z, Candela PA, Piccoli PM, Sanchez-Valle C (2012) The partitioning of sulfur and chlorine between andesite melts and magmatic volatiles and the exchange coefficients of major cations. *Geochim Cosmochim Acta* 89:81–101. <https://doi.org/10.1016/j.gca.2012.04.039>

- Zhang Y (1999) H₂O in rhyolitic glasses and melts: measurement, speciation, solubility, and diffusion. *Rev Geophys* 37:493–516. <https://doi.org/10.1029/1999RG900012>
- Zhang Y, Ni H (2010) Diffusion of H, C, and O Components in Silicate Melts. *Rev Min Geochem* 72:171–225. <https://doi.org/10.2138/rmg.2010.72.5>
- Zhang C, Holtz F, Ma C, Wolff PE, Li X (2012) Tracing the evolution and distribution of F and Cl in plutonic systems from volatile-bearing minerals: a case study from the Liujiawa pluton (Dabie orogen, China). *Contrib Min Petrol* 164:859–879. <https://doi.org/10.1007/s00410-012-0778-9>
- Zhang C, Koepke J, Albrecht M, Horn I, Holtz F (2017) Apatite in the dike-gabbro transition zone of mid-ocean ridge: evidence for brine assimilation by axial melt lens. *Am Min* 102:558–570. <https://doi.org/10.2138/am-2017-5906>